



UNIVERSITEIT•STELLENBOSCH•UNIVERSITY
jou kennisvennoot • your knowledge partner

Design and comparison of three surface-mounted PM motors for a light electric vehicle

Francois Du Plessis
20688830

Report submitted in partial fulfilment of the requirements of the module
Project (E) 448 for the degree Baccalaureus in Engineering in the Department of
Electrical and Electronic Engineering at Stellenbosch University.

Supervisor: Prof RJ Wang

November 2020

Acknowledgements

Aan Jesus Christus, my Verlosser, wat my elke dag krag gee.

Aan Carla, vir jou ondersteuning en liefde.

Aan my ouers, Fanie en Nicolene, vir my grootmaak en bring tot waar ek vandag is.

Aan Kobus, vir al jou hulp en kennis die laaste vier jaar.

To Professor Wang and Stavros Pastellides, for your guidance and support during the project.



UNIVERSITEIT • STELLENBOSCH • UNIVERSITY
jou kennisvennoot • your knowledge partner

Plagiaatverklaring / *Plagiarism Declaration*

1. Plagiaat is die oorneem en gebruik van die idees, materiaal en ander intellektuele eiendom van ander persone asof dit jou eie werk is.

Plagiarism is the use of ideas, material and other intellectual property of another's work and to present is as my own.

2. Ek erken dat die pleeg van plagiaat 'n strafbare oortreding is aangesien dit 'n vorm van diefstal is.

I agree that plagiarism is a punishable offence because it constitutes theft.

3. Ek verstaan ook dat direkte vertalings plagiaat is.

I also understand that direct translations are plagiarism.

4. Dienooreenkomstig is alle aanhalings en bydraes vanuit enige bron (ingesluit die internet) volledig verwys (erken). Ek erken dat die woordelike aanhaal van teks sonder aanhalingstekens (selfs al word die bron volledig erken) plagiaat is.

Accordingly all quotations and contributions from any source whatsoever (including the internet) have been cited fully. I understand that the reproduction of text without quotation marks (even when the source is cited) is plagiarism

5. Ek verklaar dat die werk in hierdie skryfstuk vervat, behalwe waar anders aangedui, my eie oorspronklike werk is en dat ek dit nie vantevore in die geheel of gedeeltelik ingehandig het vir bepunting in hierdie module/werkstuk of 'n ander module/werkstuk nie.

I declare that the work contained in this assignment, except where otherwise stated, is my original work and that I have not previously (in its entirety or in part) submitted it for grading in this module/assignment or another module/assignment.

20688830 Studentenommer / Student number	<i>F. Du Plessis</i> Handtekening / Signature
F. Du Plessis Voorletters en van / Initials and surname	2020-11-08 Datum / Date

Abstract

English

This report details the design, analysis and comparison of three surface mounted permanent magnet synchronous motors which feature fractional-slot windings. The concepts surrounding electric vehicles, traction requirements, permanent magnet technology and winding topologies are introduced and discussed. Specifically, the concept of fractional-slot windings, both concentrated and distributed windings, is introduced. Operational principles of surface mounted permanent magnet synchronous motors are introduced and discussed along with flux weakening operation of these machines. A design method is proposed and implemented to obtain initial machine dimensions before the machine dimensions are optimised to find the lowest cost at which all constraints are satisfied. Finite-element analysis is used to evaluate machine performance and compare the chosen winding topologies. The conclusion is drawn that the double-layer concentrated winding machine provides the best performance w.r.t. cost, with the distributed winding machine performing marginally worse taking cost into account.

Afrikaans

Hierdie verslag beskryf die ontwerp, analise en vergelyking van drie oppervlak gemonteerde permanente magneet sinchroon motors met breukdeel gleuf windings (FSCW). Die konsepte rakende elektriese motors (karre), trekkrag vereistes, permanente magneet tegnologie and winding uitleg word bekendgestel en bespreek. The konsep van breukdeel gleuf windings, beide gekonsentreerde en verspreide windings, word bekendgestel en bespreek. Operationele beginsels van permanente magneet sinchroon motors word bekendgestel en bespreek asook vloed verswakkende beheer en operasie. 'n Ontwerps prosedure word voorgestel en uitgevoer om aanvanklike masjien dimensies te vind voor 'n optimiseringsproses uitgevoer word om die laagste moontlike kostepunt te vind waarby alle beperkings bevredig word. Eindige-element analise word gebruik om masjien prestasie te evalueer en om die gekose winding topologië te vergelyk. Daar word tot die gevolgtrekking gekom dat die dubbel laag gekonsentreerde winding masjien die beste presteer t.o.v. koste, terwyl die verspreide winding masjien marginaal slegter vaar met koste in ag geneem.

Contents

Declaration	ii
Abstract	iii
List of Figures	vii
List of Tables	ix
Nomenclature	xi
1. Introduction	1
1.1. Background of the project	1
1.2. Objectives of the project	1
1.3. Scope of the project	1
1.4. Layout of the report	2
2. Traction motor drive-train systems	3
2.1. Traction efforts and vehicle physics model	3
2.2. Typical EV drive train systems	4
2.3. Common permanent magnet motor topologies	5
2.3.1. Surface-mounted PM motors (SPM)	6
2.3.2. Interior PM motors (IPM)	6
2.4. Surface-mounted PM motor technologies and fractional-slot machines . . .	7
2.5. Choice of topology	9
3. Characteristics of PM traction motors	10
3.1. Electromagnetic principles of PM motors	10
3.1.1. Open circuit magnetic field, flux linkage and back-EMF	10
3.1.2. Phase inductance, winding resistance and iron losses	11
3.2. Flux weakening operation of PM traction motors	12
3.2.1. CPSR and torque angle characteristics	14
4. Design procedure of PM motor	16
4.1. Design process and specifications for the study	16
4.2. Pole and slot combinations	17
4.3. Winding layouts	19

4.3.1. Winding layout: 12-slot 10-pole machine	20
4.3.2. Winding layout: 36-slot 8-pole machine	20
4.4. Initial sizing of design parameters	22
4.4.1. Geometric dimensions	22
4.4.2. Calculation of number of turns per phase	24
4.5. Additional considerations for final design	25
4.5.1. Cogging torque and torque ripple	25
4.5.2. Demagnetization aspects	26
4.6. Optimum design of PM motors	27
4.6.1. Formulation of optimisation problem	27
4.6.2. Finite element based optimisation process	28
4.6.3. Finite element based simulation methods	29
5. Comparative study of two SPM motors	30
5.1. Dimensions, inductance and cost	30
5.2. Main performance characteristics	32
5.2.1. Losses and efficiency	33
5.2.2. Flux linkage, voltage and current	35
5.2.3. Output torque, torque ripple and cogging torque	38
5.2.4. Demagnetisation and flux densities	38
6. Conclusion and Further work	40
6.1. Conclusion	40
6.2. Recommendations for future work	40
Bibliography	41
A. Project Planning Schedule	45
B. Outcomes Compliance	47
B.1. ELO 1: Problem solving	47
B.2. ELO 2: Application of scientific and engineering knowledge	47
B.3. ELO 3: Engineering design	48
B.4. ELO 4: Investigations, experiments and data analysis	48
B.5. ELO 5: Engineering methods, skills and tools, including Information Tech- nology	48
B.6. ELO 6: Professional and technical communication	49
B.7. ELO 8: Individual work	49
B.8. ELO 9: Independent Learning Ability	49

C. Additional results, equations and derivations	50
C.1. Flux density, thermal(current) aspects and efficiency maps	50
C.2. Results from SEMFEM simulations	50
C.3. Electrical steel properties	55
C.4. Open circuit magnetic field calculation	55
C.5. Additional inductance and resistance calculations	56
D. MATLAB design scripts	57
E. SEMFEM simulation code	61

List of Figures

2.1. Vehicle movement models	3
2.2. EV drive trains	5
2.3. Energy conversion system and drive train	5
2.4. PM motor magnet configurations (4-pole machines)	7
2.5. Winding topologies for a 4 pole machine: (a) Overlapping distributed winding ($q = 2$) (b) Overlapping concentrated winding ($q = 1$) (c) Non-overlapping winding with all teeth wound(double-layer) ($q = 0.5$) (d) Non-overlapping winding with alternate teeth wound(single-layer) ($q = 0.5$) . . .	8
3.1. Winding coil diagrams	11
3.2. Additional dimensions	12
3.3. dq-equivalent circuits	13
3.4. Voltage and current behaviour over speedrange	15
3.5. Voltage and current behaviour over speed range	15
3.6. Torque angle characteristic	15
4.1. Design process	17
4.2. Winding factors for different slot(N_s) and pole (P) combinations.	19
4.3. Winding layouts for 12-slot 10-pole machine	21
4.4. Phasor diagrams	21
4.5. Double-layer winding of 36-slot 8-pole machine	21
4.6. Slot dimensions as used for initial geometric sizing	24
4.7. Demagnetization characteristics	27
4.8. Optimisation process	28
4.9. Delta-wye connection of motor	29
5.1. Slot dimensions	30
5.2. Preliminary optimised machines	32
5.3. Mesh used in SEMFEM	32
5.4. Mesh used in ANSYS Maxwell	32
5.5. Magnet losses at 1500 rpm	33
5.6. Magnet losses at 5000 rpm	34
5.7. Flux linkage at 1500 rpm	34
5.8. Induced voltage (back-emf) at 1500 rpm	35

5.9. Flux linkage at 5000 rpm	36
5.10. Induced voltage (back-emf) at 5000 rpm	36
5.11. Phase current at 1500 rpm	36
5.12. Phase current at 5000 rpm	37
5.13. Output torque at 1500 rpm	37
5.14. Output torque at 5000 rpm	37
5.15. Mesh used for cogging torque determination	38
5.16. Cogging torque	39
5.17. Flux densities of 12-slot machines at 1500 rpm	39
5.18. Flux densities of 36-slot machine	39
A.1. Initial planning	45
A.2. Revised planning	46
C.1. Flux densities of 12-slot machines at 5000 rpm	51
C.2. Efficiency map of 12-slot single-layer machine	51
C.3. Loss map of 12-slot single-layer machine	52
C.4. Efficiency map of 12-slot double-layer machine	52
C.5. Loss map of 12-slot double-layer machine	53
C.6. Efficiency map of 36-slot machine	53
C.7. Loss map of 36-slot machine	54
C.8. M19_26G BH-curve	54
C.9. Machine dimensions	56

List of Tables

4.1. Dimensions and specifications of EV drive train	17
4.2. Dimensions and specifications of SPM	18
4.3. Possible winding layouts	18
4.4. Winding factors	22
4.5. Current limits for air-cooled PMSMs	22
4.6. Input parameters for design at 1500 rpm	22
4.7. Initial geometric parameters	25
4.8. Cogging torque parameters	26
4.9. dq-current densities of machines	29
5.1. Inductances of machines	31
5.2. Main machine dimensions	31
5.3. Slot parameters	31
5.4. Cost and mass of final machines	31
5.5. Results at 1500 rpm	33
5.6. Results at 5000 rpm	34
5.7. Phase angle of terminal voltages	35
5.8. Cogging torque of different machines	38
C.1. Current limits for air-cooled PMSMs	50
C.2. Preliminary design results at 1500 rpm (SEMFEM)	51
C.3. Preliminary design results at 5000 rpm (SEMFEM)	54

Nomenclature

Variables and functions

A_{Cu}	Copper conductor area.
A_f	Frontal area of vehicle.
A_{slot}	Slot area.
A_{us}	Usable slot area.
$B_{airgap}(r, \theta)$	Air-gap flux density considering slotting effects.
B_g	Approximate air gap flux density amplitude.
B_{g1}	Fundamental air gap flux density amplitude.
\hat{B}_m	Peak air-gap flux density.
B_{MM}	Magnetisation margin.
B_r	Remnant magnet flux density.
$B_{slotless}(r, \theta)$	Air-gap flux density neglecting slotting effects.
B_{ts}	Stator tooth magnetic flux density.
B_{yr}	Rotor yoke magnetic flux density.
B_{ys}	Stator yoke magnetic flux density.
C_D	Aerodynamic Drag coefficient.
C_T	Cogging torque factor.
D_{ag}	Air gap diameter.
D_{er}	External rotor diameter.
D_{h1}	Diameter after slot enclosure.
D_{is}	Internal stator diameter.
D_{out}	Stator outer diameter.
D_{shaft}	Shaft diameter.
E_m	Phase back EMF (RMS).
E_{rated}	Open circuit rated line to neutral, RMS voltage.
e_{RMS}	Line-to-neutral phase back EMF (RMS).
f, f_e	Electrical frequency.
f_{Brn}	Air-gap flux density coefficient.

f_f	Slot fill factor.
F_r	Rolling resistance.
f_r	Rolling resistance coefficient.
F_t	Tractive effort.
F_w	Aerodynamic drag.
g	Air gap length.
g_{grav}	Gravitational acceleration (9.81 m/s ²).
g_{eff}	Effective air gap.
h_m	Magnet thickness.
h_{ys}	Stator yoke height.
h_{us}	Usable slot height.
h_1	Slot enclosure depth.
I_{ch}	Characteristic current.
i_d	d-axis current.
i_g	Gear ratio.
I_{max}	Maximum phase current.
i_o	Differential ratio.
i_q	q-axis current.
I_R	Rated phase current.
I_S	Phase current.
J	Winding current density.
K_{Bn}	Air-gap flux density coefficient.
K_c	Carter factor.
k_j	Stacking factor.
K_s	Linear current density.
K_{wn}	n^{th} harmonic winding factor.
k_{wv}	v^{th} harmonic winding factor.
K_{w1}	Fundamental winding factor.
K_{CPSR}	Constant power speed range ratio.
L, l	Length of stator.
l_c	Approximate coil length.
L_d	d-axis inductance.
l_{ew}	End winding length.

L_{ew}	End winding leakage inductance.
L_h	Harmonic leakage inductance.
L_L	Leakage inductance.
L_m	Magnetizing inductance.
L_q	q-axis inductance.
L_s	Synchronous inductance.
l'	Effective stator length.
L_σ	Slot leakage inductance.
m	Number of phases.
M_v	Vehicle mass.
N	Cogging torque factor.
N_c	Number of turns per coil.
N_C	Smallest common multiple of Q_s and $2p$.
N_p	Rotational speed of electric motor shaft.
N_{ph}, N_s	Number of turns per phase.
p	Number of pole pairs.
P_{Core}	Core losses.
P_{Cu}	Copper losses.
P_{Fe}	Iron losses.
P_{in}	Electrical input power.
P_{loss}	Peak total electrical losses.
P_{magnet}	Magnet losses.
P_{out}	Electric motor output power.
q	Number of slots per pole and phase.
Q, Q_s	Number of stator slots.
r_d	Wheel radius.
R_{DC}	DC winding resistance neglecting skin effect.
R_{is}	Radius of inner stator.
R_s	Stator winding resistance.
t	Time/winding periodicity.
T_{MG}	Output torque of magnetic gear.
T_p	Output torque from electric motor.
T_r	Rated torque at base speed.

T_{rip}	Torque ripple.
$T_{winding}$	Winding temperature.
V	Vehicle speed.
v_{an}	Line-to-neutral terminal voltage.
v_d	d-axis terminal voltage.
V_{max}	Maximum terminal voltage.
v_q	q-axis terminal voltage.
W	Coil pitch in unit of length.
W_{ew}	End winding width.
w_{sb}	Bottom slot width.
w_{st}	Top slot width.
w_{tt}	Top tooth width.
w_0	Slot opening width.
z_Q	Number of conductors per slot.
z_{wire}	Number of wires per conductor.
α_p	Magnet pitch to pole pitch ratio.
α_u	Slot pitch angle.
β_T	Current angle.
γ	Chosen coil pitch in number of slots.
γ_Q	Calculated coil pitch in number of slots.
δ_{RF}	Torque angle.
η	Motor efficiency.
η_t	Drive train efficiency.
θ	Mechanical angle.
θ_{deg}	Phase angle in degrees.
θ_{elec}	Electrical angle.
θ_{mech}	Mechanical angle.
λ	Flux linkage.
λ_a	Armature flux linkage.
λ_{coil}	Coil flux linkage.
λ_d	d-axis flux linkage.
λ_{ew}	End winding permeance factor.
λ_{phase}	Phase flux linkage.

λ_{PM}	Permanent magnet flux linkage.
λ_q	q-axis flux linkage.
$\lambda_{rel}(\theta)$	Relative permeance function.
λ_w	End winding permeance factor.
μ_r	Relative permeability.
μ_0	Magnetic permeability of free space ($4\pi \times 10^{-7} H/m$).
ρ_{air}	Air density ($1.225 \text{ kg}/m^3$).
ρ_{Cu}	Copper resistivity ($0.0171 \Omega \cdot mm^2/m$).
ρ_{Fe}	Electrical steel resistivity.
σ_u	Slot leakage factor.
τ_p	Pole pitch.
τ_s	Slot pitch angle.
ϕ_P	Air-gap flux per pole
ϕ_{rot}	Flux in rotor.
ψ	Length-diameter ratio.
ω_e	Angular electrical frequency.
ω_{mech}, ω_p	Rotational speed of electric motor shaft.

Acronyms and abbreviations

CPSR	Constant power speed range
CTSR	Constant torque speed range
dq	direct-quadrature
EMF	Electromotive force
EV	Electric vehicle
FEA	Finite element analysis
FEM	Finite element method
FSCW	Fractional slot concentrated winding
FSDW	Fractional slot distributed winding
GCD	Greatest common divisor
IMD	Integrated motor drive
IPM	Interior permanent magnet motor
LEV	Light electric vehicle
MMF	Magnetomotive force
PM	Permanent magnet
PMSM	Permanent magnet synchronous motor
RBPM	Radial-bar permanent magnet motor
RMS	Root mean square
SBM	Surface buried permanent magnet motor
SMC	Soft magnetic composite
SPM	Surface mounted permanent magnet motor
STPM	Spoke-type permanent magnet motor
VPM	V-shaped permanent magnet motor

Chapter 1

Introduction

1.1. Background of the project

Globally, there are increasing concerns surrounding climate change, fossil fuel supply and energy security [1]. With transportation predicted to contribute 50% of global greenhouse emissions by 2030 [2], electric vehicles (EVs) offer the potential to reduce the environmental impact of transportation and increase energy independence, if paired with renewable energy infrastructure. High-performance electric vehicle drive motors are one of the critical components needed for the widespread adoption of EVs. Permanent magnet synchronous motors (PMSM) have been widely adopted in recent years for their simple structure and high efficiency. However, several aspects require more research [3]. Additional technologies such as integrated motor drives (IMDs) offer significant advantages when combined with PMSMs [4], [5].

1.2. Objectives of the project

The main objective of the project is to carry out a comparative study on different configurations of surface-mounted PMSMs through the use of FEA software, with the intended application in a light electric vehicle (LEV) as described in [6]. This study must highlight the advantages of the different configurations and evaluate the performance thereof. Secondary to this, a design procedure must be developed and implemented for the design of the different machines which is reproducible and takes into account practical considerations regarding aspects such as manufacturing.

1.3. Scope of the project

The project involves the design and comparison of three surface-mounted PMSMs through the use of FEA software, designed under the assumption of flux-weakening control. The machines are not to be built for this study, however practical considerations are to be taken into account. While additional concepts such as EV drive trains and magnetic gears are discussed, these are not the focus of this project. In-depth demagnetisation analysis is

not to be carried out. While harmonic content is minimised by machine choice, harmonic analysis of the machines is not carried out. Thermal aspects are considered, but a detailed analysis of the thermal aspects of the final machines is not carried out.

1.4. Layout of the report

The report will be structured as follows:

- Chapter 2 provides the necessary background information to understand EV traction requirements, drive train configurations as used in the broader project, PM technologies and winding configurations focusing on introducing fractional-slot concentrated winding machines to the reader.
- Chapter 3 gives an overview of the electromagnetic principles of PMSMs. Properties such as inductance, resistance and losses are discussed with a focus on these quantities as found in fractional-slot machines. Flux-weakening operation is discussed, the concept of a constant power speed range is introduced and torque angle characteristics are discussed.
- Chapter 4 provides detail on the design procedure followed including the selection of machines w.r.t pole and slot combinations, winding layouts, initial machine sizing and the optimisation procedure implemented to find the optimal design. Additional considerations such as cogging torque and demagnetisation are discussed along with simulation specific parameters.
- Chapter 5 presents the results obtained from both FEA software packages used, one in-house package and the commercial standard, provides a discussion of these results and possible reasons for performance characteristics.
- Chapter 6 provides a summary of the project, a conclusion regarding the comparative study of the machines and possible improvements and recommendations for future work.

Chapter 2

Traction motor drive-train systems

This chapter describes the vehicle physics model and tractive effort, typical EV drive train systems and electric motor topologies. SPM technologies and winding topologies are also introduced and discussed.

2.1. Traction efforts and vehicle physics model

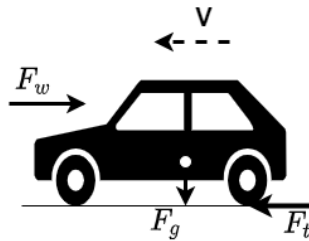
The vehicle movement model with forces acting on the vehicle is shown in Fig. 2.1. The tractive effort, F_t , is the force that propels the vehicle forward and acts on the vehicle at the contact area between the tyres and the driving surface. Acting in the opposite direction to vehicle movement is aerodynamic drag, F_w , and rolling resistance, F_r , given by Eq. 2.1 and Eq. 2.2 respectively [7]. Applying Newton's second law under the condition of zero acceleration, Eq. 2.3 is obtained.

$$F_w = \frac{1}{2} \rho_{air} C_D A_f V^2 \quad (2.1)$$

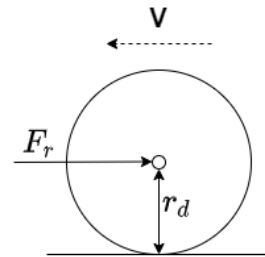
$$F_r = M_v g_{grav} f_r \quad (2.2)$$

$$F_t = F_w + F_r \quad (2.3)$$

The torque produced by the electric motor, T_p , is related to F_t by Eq. 2.4, with i_g , i_o , η_t the magnetic gear ratio, differential gear ratio and the drive train efficiency respectively.



(a) Vehicle model



(b) Model of wheel with rolling resistance indicated

Figure 2.1: Vehicle movement models

$$F_t = \frac{T_p i_g i_o \eta_t}{r_d} \quad (2.4)$$

The maximum rotational speed of the motor can be found using Eq. 2.5, with $N_{p(max)}$, V_{max} the maximum rotational speed of the motor in revolutions per minute (rpm) and the maximum speed of the vehicle respectively. The power of the electric motor can be obtained through Eq. 2.6, with P_{out} , $\omega_{p(max)}$ the output power of the electric motor and the maximum rotational speed of the motor in rad/s respectively .

$$V_{max}(m/s) = \frac{\pi N_{p(max)} r_d}{30 i_g i_o} \quad (2.5)$$

$$P_{out} = T_{p(min)} \omega_{p(max)} \quad (2.6)$$

2.2. Typical EV drive train systems

Typical drive train layouts for EV's are shown in Fig. 2.2 [7]. Note that all layouts are for rear-wheel drive vehicles. Fig. 2.2a shows the layout typically associated with an internal combustion engine vehicle, with the engine replaced with an electric motor. Fig. 2.2b features a similar layout to Fig. 2.2a, however the clutch is removed as the gearbox now has a fixed transmission ratio. Fig. 2.2c shows a layout where the drive train components are combined into a single unit, with both axle sides connected to the wheels through a differential and fixed speed gearbox. Fig. 2.2d shows a layout where each of the rear-wheels is driven by an independent motor-gearbox combination. Fig. 2.2e is very similar, with the exception that the fixed speed gearbox is now integrated into the wheel assembly. Lastly, Fig. 2.2f shows a layout where the electric motor is directly integrated into the wheel assembly, through the use of an outer rotor motor. An expanded diagram of the energy conversion system similar to Fig. 2.2b is shown in Fig. 2.3 [7]. A version of this system is to be implemented in this project, using a magnetic gear [8] with a fixed ratio and combining the power electronics and motor into a single assembly, called an integrated motor drive (IMD) [4], [5]. The magnetic gear limits the maximum torque production of the motor, as shown in Eq. 2.7, with $T_{MG(max)}$ the maximum output torque of the magnetic gear. With the output power known from Eq. 2.6 and the maximum torque chosen to be less than $T_{p(max)}$, the base speed, $\omega_{p(base)}$, can be obtained from Eq. 2.8.

$$T_{p(max)} = \frac{T_{MG(max)}}{i_g} \quad (2.7)$$

$$\omega_{p(base)} = \frac{P_{out}}{T_{p(max)}} \quad (2.8)$$

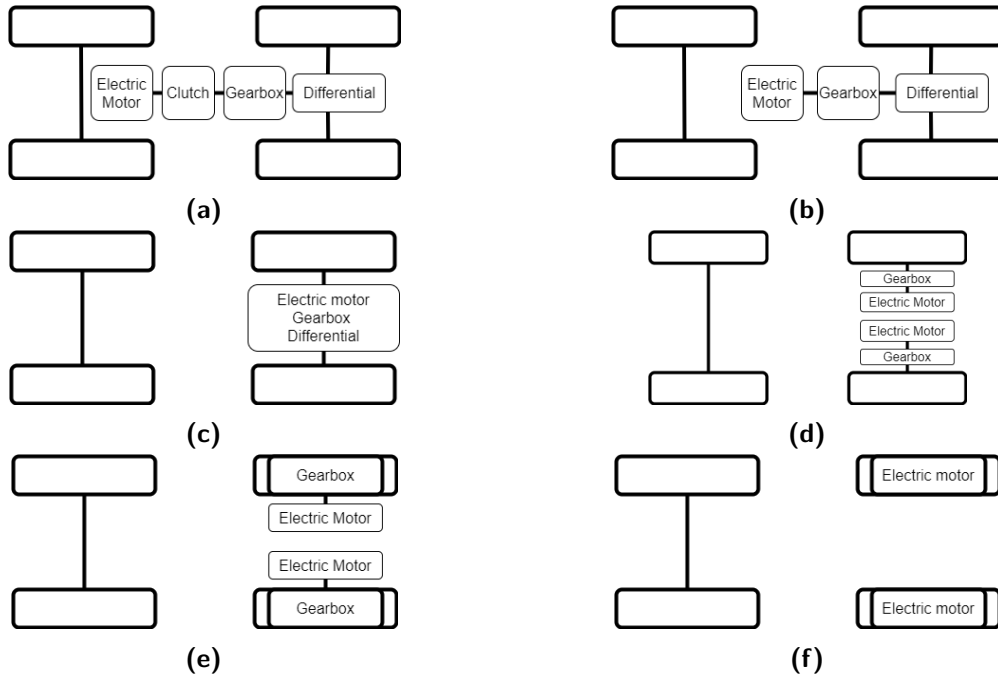


Figure 2.2: EV drive trains

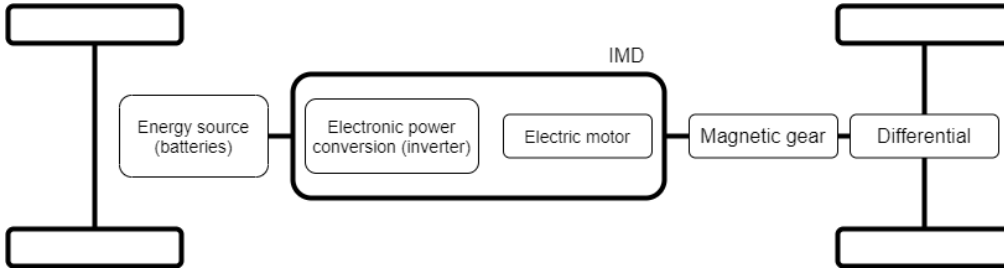


Figure 2.3: Energy conversion system and drive train

2.3. Common permanent magnet motor topologies

Substituting conventional field windings with permanent magnets gives the advantage of reduced copper losses and increased reliability due to the removal of brushes [9]. Neodymium iron boron (NdFeB) magnets are the most powerful magnets available - providing the strongest magnetic field per unit volume [10]. Accordingly, these magnets enable a reduction in magnet volume for the same magnetic field strength and reduce machine size [11]. However, these magnets may vary in price and availability due to supply-chain concentration and volatility of the rare-earth elements [11]. Various efforts have been made to find alternatives, including recycling magnets and using ferrite magnets, but NdFeB magnets remain dominant [11], [12]. There are many different PM rotor topologies for PM motors, some of which are shown in Fig. 2.4. These can be split into two main categories, i.e. surface-mounted and interior PM motors.

2.3.1. Surface-mounted PM motors (SPM)

The main advantages offered by SPMs are low cost due to simplistic manufacturing and high performance, as the main field produced by the magnets is practically in the air gap of the machine and leakage flux is reduced [9], [13]. Since the magnets have a permeability very close to air and are mounted on a cylindrical rotor, there is very little difference between the d-and q-axis inductances, known as magnetic saliency [9], [13]. This may have control and operational implications [13] but high quality torque and EMF is produced. The major disadvantage is the risk of demagnetization, explained in Section 4.5.2, due to the exposure of the magnets to very strong fields produced by the stator windings [9]. Another disadvantage is that SPMs with conventional stator windings typically have low inductance values and are thus considered to be ill suited for flux weakening operation [9], [14]. Fractional slot concentrated windings (FSCW) offer a potential solution, explained in more detail in Section 2.4. SPM machines may also require additional mechanical strengthening to prevent displacement of magnets mounted to the rotor surface in high speed applications.

2.3.2. Interior PM motors (IPM)

IPMs require more complex rotor design with features such as cutouts in the rotor laminations to fit the magnets and flux barriers, as shown in Fig. 2.4b. These motors exhibit a larger magnetic saliency compared to SPMs, resulting in a higher reluctance torque in addition to the magnetic torque [13]. IPMs may also produce more noise than SPMs, although this can be mitigated by stator tooth shaping [15]. Several IPM topologies are shown in Fig. 2.4. Surface buried PM motors (SBM) are similar to SPMs with the difference being the magnets placed under a thin layer of laminations near the rotor surface. Using air gap flux barriers, a nearly constant flux distribution on the surface of the rotor can be obtained, producing high quality torque and EMF [9]. The laminations shield the PMs from stator fields, reducing the risk of demagnetization. These type of motors are similar to radial-bar PM motors (RBPM), which also feature a higher flux weakening capability compared to other IPM types [13]. Spoke-type PM motors (STPM) provide the highest torque and flux density of PM machines [16]. However, these types of PM motors offer reduced flux weakening capability, a lower reluctance torque due to reduced magnetic saliency, and are more susceptible to demagnetisation [16]. V-shaped PM motors (VPM) provide the ability to adjust the flux concentration and the saliency ratio of the dq-inductances by adjusting the angle of the V-shaped magnets [13]. These motors exhibit good performance in torque applications and wide speed range operation [13].

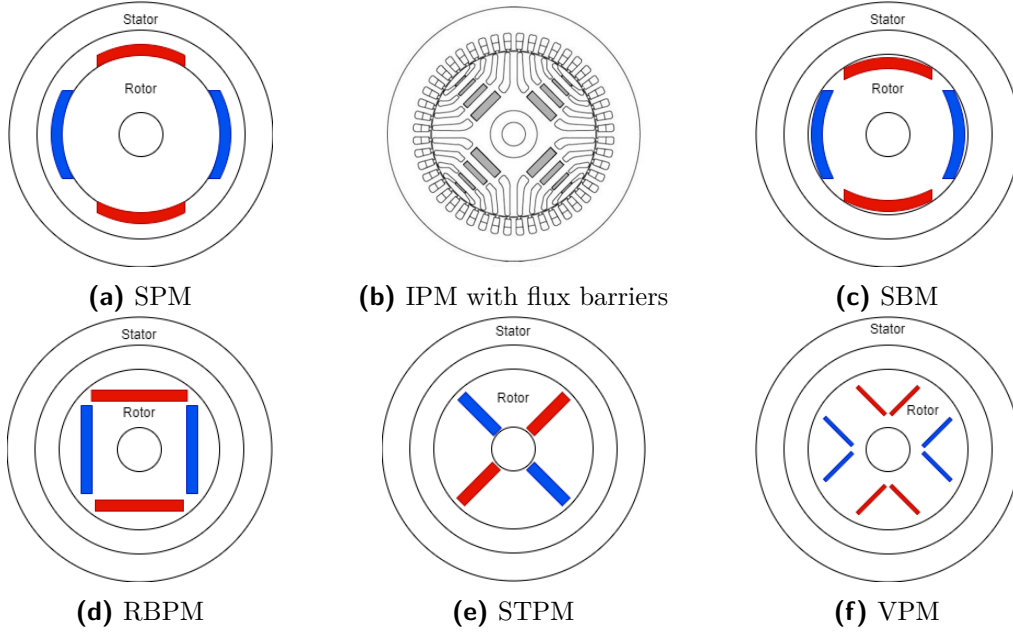


Figure 2.4: PM motor magnet configurations (4-pole machines)

2.4. Surface-mounted PM motor technologies and fractional-slot machines

Fractional-slot machines are defined as machines where the number of slots per pole and phase, q , is not an integer. Subsequently, the two categories of fractional-slot machines are defined as follows for the rest of this report:

- FSCW: A machine with $q < 1$ and windings on all teeth or on alternate teeth i.e. windings encircle only a single stator tooth and are non-overlapping.
- FSDW: A machine with $q > 1$ and $q \notin \mathbb{N}$, where \mathbb{N} is the set of natural numbers, and where windings encircle more than one tooth.

Different winding configurations are shown in Fig. 2.5 with their respective q values [15]. Note that FSCW machines with windings on alternate teeth are referred to as single-layer windings, while those with windings on all teeth are referred to as double-layer windings [15]. FSCW PM machines offer several advantages: high power density due to high slot fill factors, short end turns which reduce copper losses and increase efficiency, low cogging torque, flux weakening capability and fault tolerance [15]. Distributed overlapping windings, both FSDW and conventional, are used in PM machines as they generally provide a more sinusoidal MMF distribution and EMF waveform [15]. FSCW reduce losses due to shorter end windings which also reduces cost due to copper volume reduction [15]. Simpler manufacturing and increased slot fill factors are possible when segmented stator structures are used, especially with soft magnetic composite(SMC), plug-in teeth and

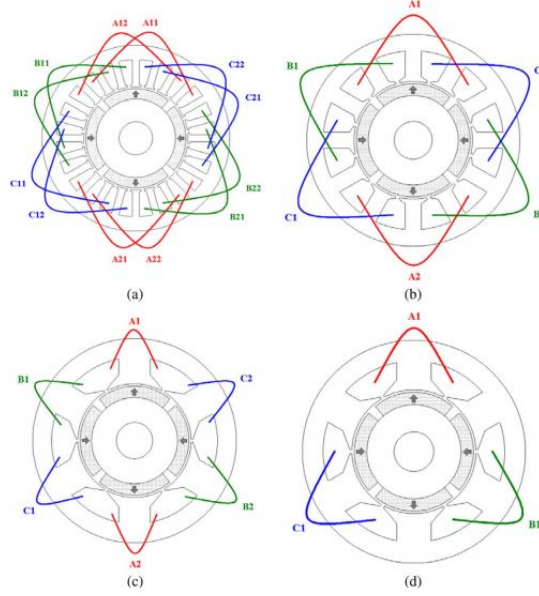


Figure 2.5: Winding topologies for a 4 pole machine: (a) Overlapping distributed winding ($q = 2$) (b) Overlapping concentrated winding ($q = 1$) (c) Non-overlapping winding with all teeth wound(double-layer) ($q = 0.5$) (d) Non-overlapping winding with alternate teeth wound(single-layer) ($q = 0.5$)

joint-lapped core structures. By increasing the slot fill factor, f_f , as defined in Eq. 2.9 the power density is increased [15]. Note A_{Cu} and A_{slot} are the copper conductor areas and slot areas respectively.

$$f_f = \frac{A_{Cu}}{A_{slot}} \quad (2.9)$$

FSCWs may have higher inductance values compared to distributed winding SPMs due to high harmonic leakage inductance [14]. This increases flux-weakening capability by decreasing the characteristic current, I_{ch} , as defined in Eq. 2.10, and increases the constant power speed range (CPSR). Optimal flux-weakening occurs when $I_{ch} = I_R$, as the symmetrical three-phase short-circuit current will equal the rated current, I_R . However, this condition will cause demagnetization, based on Fig. 3.3c and Fig. 3.3 [6].

$$I_{ch} = \frac{\lambda_{PM}}{L_d} \quad (2.10)$$

Fault tolerance requirements include electrical, magnetic, thermal and physical separation between phases. It is clear that these requirements are best met by the single-layer FSCW machine, where the windings are physically separate and there is very low mutual coupling between phases, yet high self-inductance which limits current. Making use of IMD technology and feeding each phase from a separate, single-phase inverter further increases fault tolerance [15]. FSCWs suffer from two potential disadvantages. Rotor losses are significantly higher due the high harmonic content (both sub and super space harmonics) and increase as the rotational speed increases. These losses include rotor iron losses, PM

losses and losses in conducting retaining sleeves in SPM's. Single-layer windings further increase losses due to increased harmonic content. FSCW may also have higher levels of parasitic effects which include vibration and noise, unbalanced magnetic forced and torque ripples [15].

Single- and double-layer windings both offer advantages. Since single-layer windings only have one coil side/slot, manufacturing is simplified and better fault tolerance is achieved. Single-layer windings also provide higher self-inductance and thus better flux weakening capability. Double-layer windings provide lower rotor losses, more possible pole and slot combinations and a more sinusoidal back-EMF waveform due to a lower winding factor compared to single-layer windings. This lower winding factor can mean lower torque performance compared to single-layer winding machines [15].

2.5. Choice of topology

The SPM magnet topology is chosen for this design study due to its simplistic manufacturing and good performance characteristics. It will be paired with both FSCW and FSDW machines, with the FSDW machine serving as conventional benchmark. A single- and double-layer FSCW machine with the same slot-pole combination will be studied, to make a comparison w.r.t. performance.

Chapter 3

Characteristics of PM traction motors

This chapter introduces the electromagnetic principles governing the operation of SPMs, describes characteristic quantities such as inductance, resistance and losses and introduces flux weakening operation.

3.1. Electromagnetic principles of PM motors

The basic working principle of a three-phase PM synchronous motor can be explained as follows. Three-phase alternating current is applied to the armature windings in the stator, producing a rotating magnetic field. The field produced by the magnets on the rotor, tends to align with this rotating magnetic field and thus rotation is produced. Once the rotor rotates in synchronism with the rotating magnetic field, a steady electromechanical torque is produced in addition to an induced voltage in the armature windings [17].

3.1.1. Open circuit magnetic field, flux linkage and back-EMF

Although FEA provides the most accurate results for quantities such as the magnetic flux density in the air gap, analytical methods can be applied [18], [19]. The air gap flux density distribution can be calculated from Eq. 3.1, neglecting the effect of slotting. Note that θ is in mechanical radians and coefficients are calculated in Appendix C.

$$B_{slotless}(r, \theta) = \sum_{n=1,3,5\dots}^{\infty} K_{Bn} f_{Bn} \cos(np\theta) \quad (3.1)$$

From [18], it is known that for FSCW machines, maximum flux linkage occurs when the center of the magnet pole aligns with the center of the stator tooth around which the coil is wound, as shown in Fig. 3.1a. From Fig. 3.1a and Eq. 3.1, the coil flux linkage can be calculated using Eq. 3.2, with $\gamma = 1$. This equations can also be applied to FSDW machines. The flux-linkage per phase is given by Eq. 3.3 [18], [17]. The back-EMF is given by Eq. 3.4. Note the amplitude of the air-gap flux density is assumed to be constant, and thus the back-EMF consists only of a speed voltage, induced in the stator windings by the relative motion of the air-gap flux wave [17].

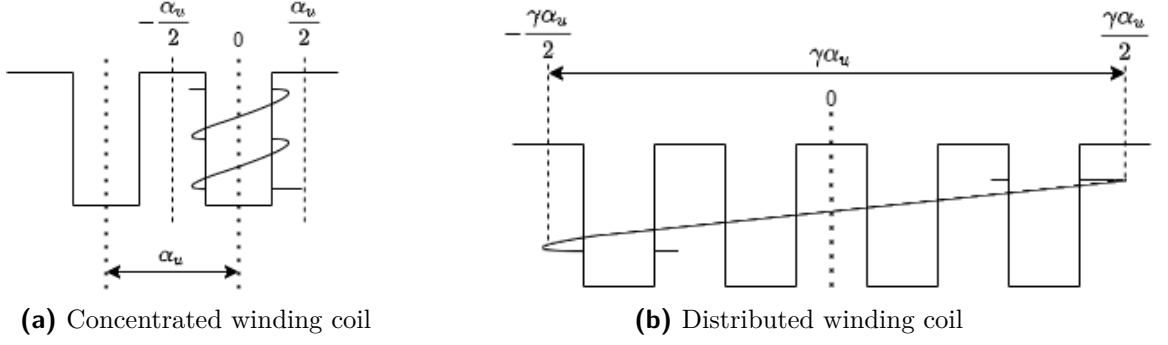


Figure 3.1: Winding coil diagrams

$$\lambda_{coil} = N_c L R_{is} \int_{-\frac{\gamma\alpha_u}{2}}^{\frac{\gamma\alpha_u}{2}} B_{slotless}(R_{is}, \theta) d\theta \quad (3.2)$$

$$\lambda_{phase} = 2N_{ph} L R_{is} \sum_{n=1,3,5,\dots}^{\infty} \frac{1}{np} K_{wn} K_{Bn} f_{Brn} \cos(np\theta) \quad (3.3)$$

$$\begin{aligned} EMF &= -\frac{d\lambda_{phase}}{dt} \\ &= 2N_{ph} L R_{is} \omega_{mech} \sum_{n=1,3,5,\dots}^{\infty} K_{wn} K_{Bn} f_{Brn} \sin(np\omega_{mech}t) \end{aligned} \quad (3.4)$$

3.1.2. Phase inductance, winding resistance and iron losses

The synchronous inductance mainly consists of the magnetizing inductance, L_m , slot leakage inductance, L_σ , end-winding inductance, L_{ew} , and the harmonic leakage inductance, L_h . Analytical expressions are provided in Eq. 3.5 to Eq. 3.9, with no analytical expression provided for L_h . The end winding permeance factors, λ_{lew} and λ_w , can be found in [19] while additional information for all equations is provided in Appendix C.5. For FSDW the magnetizing inductance makes up the largest part of the synchronous inductance while for FSCW machines, the harmonic leakage inductance contributes the largest part [14]. This is evident when examining the harmonic content of the winding functions of FSCW and FSDW machines, as in [14]. For both machines, it is also possible for the slot leakage inductance to make the largest contribution if the slot dimensions are designed in such a way.

$$L_s = L_m + L_\sigma + L_{ew} + L_h \quad (3.5)$$

$$L_m = \mu_0 \frac{2m\tau_p}{\pi^2 p g_{eff}} l' (K_{w1} N_{ph})^2 \quad (3.6)$$

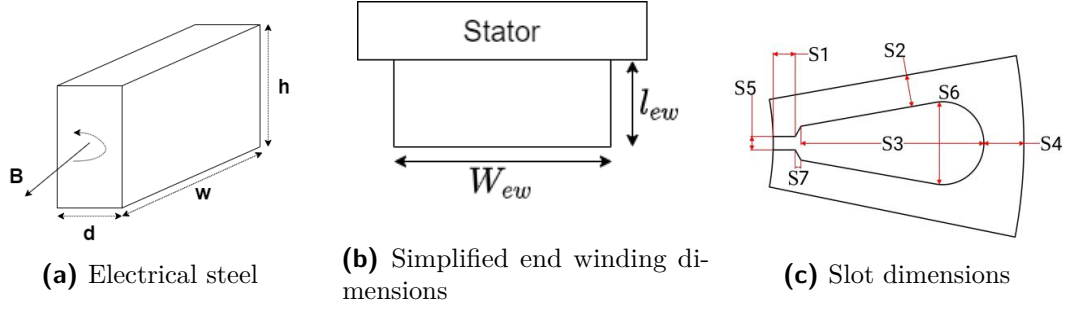


Figure 3.2: Additional dimensions

$$L_{\sigma} = \frac{4m}{Q} \mu_0 l' N_{ph}^2 \sigma_u \quad (3.7)$$

$$\sigma_u = k_1 \frac{S_3}{3S_6} + k_2 \left(\frac{S_1}{S_5} + \frac{S_7}{S_6 - S_5} \ln \frac{S_6}{S_5} \right) \quad (3.8)$$

$$L_{ew} = \frac{4m}{Q} \mu_0 q N_{ph}^2 (2l_{ew} \lambda_{lew} + W_{ew} \lambda_w) \quad (3.9)$$

The winding resistance can be calculated using Eq. 3.10, which neglects the skin effect under the assumption of small diameter wires. Iron losses are mainly caused by induced voltages in the electrical steel cores due to the alternating flux in the machine. For a sheet with dimensions as shown in Fig. 3.2a, the eddy current losses can be approximated by Eq. 3.11. As can be seen, the eddy current losses are heavily dependent on the sheet thickness, d , frequency and peak air gap flux density. These losses are mitigated by using thin steel sheets with insulation between, with the ratio of steel to insulation along the axial length of the machine, defined as the stacking factor, k_j . Other iron losses include hysteresis losses due to the alternating flux, end losses due to leakage flux penetrating the machine structure and other harmonic losses [19]. Since the PMs consist of solid material, eddy currents are induced and thus magnet losses must be considered.

$$R_{DC} = \rho_{Cu} l_c \frac{N_{ph}}{A_{Cu}} \quad (3.10)$$

$$P_{Fe} = \frac{wh\pi^2 f^2 d^3 \hat{B}_m^2}{6\rho_{Fe}} \quad (3.11)$$

3.2. Flux weakening operation of PM traction motors

Flux-weakening operation occurs between the base and maximum speeds, where negative d-axis flux is produced by the armature current to oppose the PM flux, λ_{PM} , and ensure voltage limits are not exceeded [20]. To further describe flux-weakening operation for an

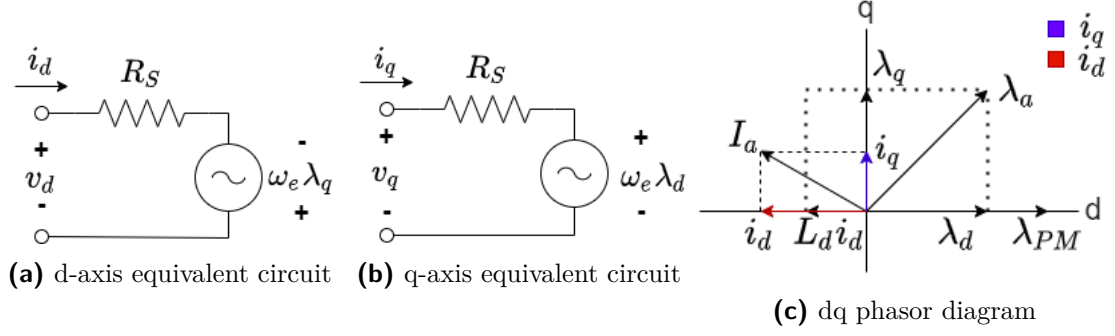


Figure 3.3: dq-equivalent circuits

SPM, the dq-reference frame, which rotates synchronously at ω_e , is used. The general dq-equivalent circuits are shown in Fig. 3.3a and Fig. 3.3b along with a dq-axis phasor diagram in Fig. 3.3c [21]. Note that phasors are not drawn to scale. As can be seen, the d-axis armature flux, $L_d i_d$, opposes λ_{PM} , decreasing the d-axis flux and ensuring voltage limits are adhered to. Neglecting the stator resistance, R_s , and substituting the expressions for the d-and q-axis flux, from Eq. 3.12 and 3.13, the circuit equations shown in Eq. 3.15 and 3.16 are obtained [6], [21], [22]. Note $L_d = L_q = L_s$ for an SPM. The torque produced by a SPM is given by Eq. 3.17, with only the q-axis current contributing to the torque as there is no reluctance torque component, due to no magnetic saliency [20]. The magnet flux linkage, λ_{PM} , is given by Eq. 3.18 with E_{rated} equal to the rated open circuit RMS, line-to-neutral voltage. The RMS armature flux linkage, $\lambda_{a(RMS)}$, can be calculated from Eq. 3.14. Should $\frac{\lambda_{a(RMS)}}{\lambda_{a(base)}} > 1$, negative d-axis current is required to reduce the flux linkage to ensure saturation does not occur and that voltage limits are adhered to [17].

$$\lambda_d = \lambda_{PM} + L_d i_d \quad (3.12)$$

$$\lambda_q = L_q i_q \quad (3.13)$$

$$\lambda_{a(RMS)} = \sqrt{\frac{\lambda_d^2 + \lambda_q^2}{2}} \quad (3.14)$$

$$v_d = -L_s i_q \omega_e \quad (3.15)$$

$$v_q = \omega_e (\lambda_{PM} + L_s i_d) \quad (3.16)$$

$$T_p = \frac{3}{2} p \lambda_{PM} i_q \quad (3.17)$$

$$\lambda_{PM} = \frac{\sqrt{2}E_{rated}}{\omega_{e(base)}} \quad (3.18)$$

Circle diagrams within the dq-current plane can be used to analyse flux weakening operation of SPMS, taking into account voltage and current limits imposed by the inverter which drives the motor [23], based on Eq. 3.19 and Eq. 3.21, which yields the current limit circle. Note V_{max} in this case is a RMS, line-to-neutral quantity. Substituting Eq. 3.15 and Eq. 3.16 into Eq. 3.19, yields Eq. 3.20 for the voltage limit circle with its center at $(-\frac{\lambda_{PM}}{L_s}, 0)$. The circle diagram is shown in Fig. 3.5a. Ideal flux-weakening operation for a finite-speed machine occurs between the blue and red points in Fig. 3.5a. However, since torque still has to be produced at the maximum speed, from Eq. 3.17, q-axis current must still be supplied and thus the red point is not reached. The input voltage and current behaviour over the speed range is shown in Fig. 3.4a and Fig. 3.4b.

$$V_{max}^2 \geq v_d^2 + v_q^2 \quad (3.19)$$

$$\left(\frac{V_{max}}{\omega_e L_s}\right)^2 \geq i_q^2 + \left(i_d + \frac{\lambda_{PM}}{L_s}\right)^2 \quad (3.20)$$

$$I_R^2 \geq i_d^2 + i_q^2 \quad (3.21)$$

From Fig. 3.5a and Eq. 3.20, the expressions for $\omega_{e(base)}$, in electrical rad/s, can be determined as shown in Eq. 3.22. Note $i_d = -I_R \sin \beta_T$ and $i_q = I_R \cos \beta_T$, where β_T is the angle by which the armature current leads the q-axis. The electrical frequency, $\omega_{e(max)}$, at maximum speed is given by Eq. 3.23 - the point where both circles meet. There is a single meeting point of the constraint circles for a finite speed motor [6]. As stated previously, this point is not reached due to torque required at the maximum speed and thus this speed is slightly higher than the actual maximum speed. It should be noted that these derivations rely on constant parameters of L_s and λ_{PM} , which may vary with flux levels [21].

$$\omega_{e(base)} = \frac{V_{max}}{\sqrt{(I_R L_s)^2 + \lambda_{PM}^2 - 2\lambda_{PM} L_s I_R \sin \beta_{T(max)}}} \quad (3.22)$$

$$\omega_{e(max)} = \frac{V_{max}}{\lambda_{PM} - I_R L_s} \quad (3.23)$$

3.2.1. CPSR and torque angle characteristics

The constant power speed range, CPSR, is the ratio between the maximum and base speeds, between which the output power is constant. Assuming $\beta_{T(max)} = 0$, constant

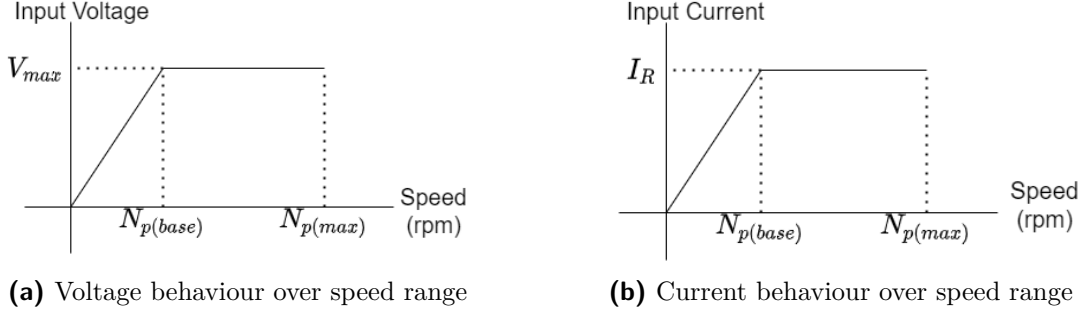


Figure 3.4: Voltage and current behaviour over speedrange

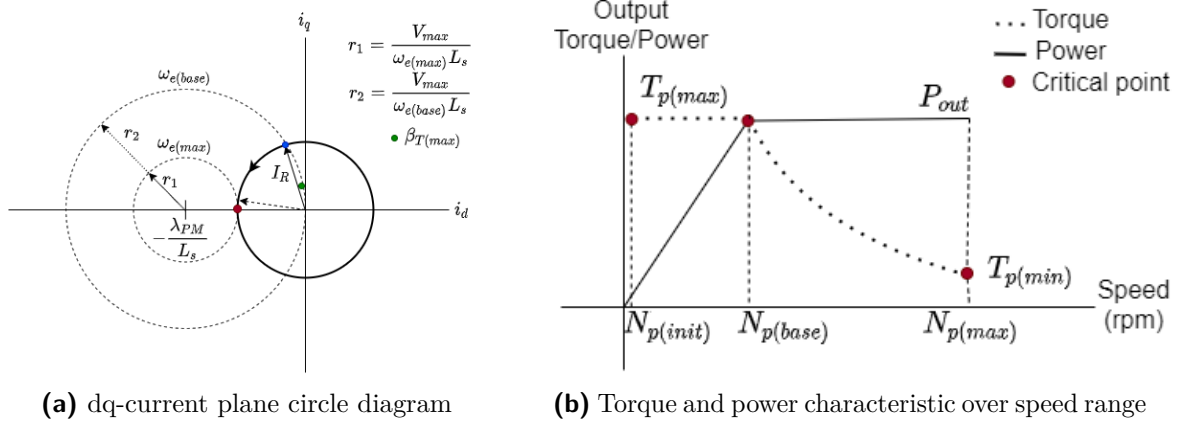


Figure 3.5: Voltage and current behaviour over speed range

power output, $i_d = 0$ at base speed and $i_q = 0$ at maximum speed, the CPSR can be defined as shown in Eq. 3.24. This expression is based on the expressions for the terminal voltage at base and maximum speed as shown in Eq. 3.22 and 3.23 respectively. Note $L_d = L_q = L_s$ and I_{max} is the peak current value. As L_s increases, the CPSR increases. Since $L_s = L_m + L_l$, either the leakage or magnetizing inductance must increase.

$$\begin{aligned}
 K_{CPSR} &= \frac{\omega_{e(max)}}{\omega_{e(base)}} \Big|_{P_{out}=Constant} \\
 &= \frac{\sqrt{(I_{max}L_s)^2 + \lambda_{PM}^2}}{\lambda_{PM} - I_{max}L_s}
 \end{aligned} \tag{3.24}$$

The torque angle characteristic of a synchronous motor is shown in Fig. 3.6 with the torque angle, δ_{RF} , defined as the electrical phase angle between the resultant air gap flux per pole, ϕ_R , and MMF of the PMs. For motors, ϕ_R leads the rotor MMF wave.

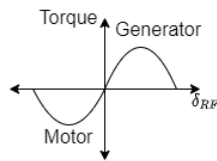


Figure 3.6: Torque angle characteristic

Chapter 4

Design procedure of PM motor

This chapter presents the design specifications obtained through equations described in Chapter 2, described the choice of slot and pole combinations, winding layouts and the initial sizing procedure of the machine. The finite element based optimisation process is also described and additional design considerations are discussed.

4.1. Design process and specifications for the study

The design process followed is shown below in Fig. 4.1. Note that optimisation is performed using an in house FEA package, SEMFEM, while analysis and verification of the designs is carried out using a commercial package, ANSYS Maxwell. Dimensions and specifications of the drive train are given in Table 4.1. From Eq. 2.5, the maximum rotational speed of the motor can be obtained with Eq. 4.1. Applying Eq. 2.3, the output torque of the motor at maximum speed can be obtained as shown in Eq. 4.2. Note the drive train efficiency is assumed to be 100 % and the mechanical differential ratio 1:1. Using Eq. 2.6, the motor power can be determined as 3076.18 W.

$$\begin{aligned} N_{p(max)} &= \frac{30i_g V_{max}}{\pi r_d} \\ &= 4879.332 \text{ rpm} \end{aligned} \quad (4.1)$$

$$\begin{aligned} T_{p(min)} &= \frac{r_d}{i_g} (M_v g_{grav} f_r + \frac{1}{2} \rho_{air} C_D A_f V_{max}^2) \\ &= 5.875 \text{ Nm} \end{aligned} \quad (4.2)$$

Choosing the output power to be 3 kW, the maximum rotational speed as 5000 rpm and considering inverter limits, the specifications of the motor are found as shown in Table 4.2. From Eq. 2.7 and Eq. 2.8, the maximum output torque of the motor is limited to 23.09 Nm while the minimum base speed is found to be 1240.7 rpm. Accordingly, the base speed and maximum torque at base speed are chosen as shown in Table 4.2. Dimensional constraints are determined by the magnetic gear shaft and casing.

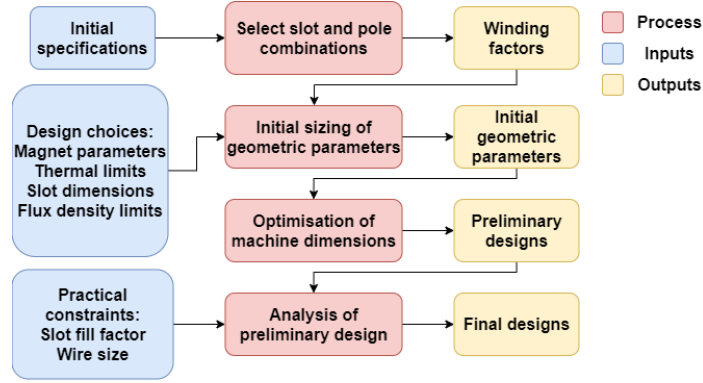


Figure 4.1: Design process

Table 4.1: Dimensions and specifications of EV drive train

Parameter	Value
Wheel radius $[r_d]$	0.299 m
Frontal area $[A_f]$	2.5 m ²
Aerodynamic drag coefficient $[C_D]$	0.3
Rolling resistance coefficient $[f_r]$	0.013
Grading percentage	0%
Vehicle mass $[M_v]$	1000 kg
Maximum vehicle speed $[V_{max}]$	50 km/h
MG ratio	11:1
Maximum MG torque $[T_{MG(max)}]$	254 Nm

4.2. Pole and slot combinations

The winding factor of a winding is the ratio between the flux linked by the winding compared to the flux linked by a single-layer full-pitch winding with $q = 1$ and the same number of turns per phase, N_{ph} , i.e. the winding factor multiplied with N_{ph} provides the effective number of turns per phase [24], [17]. Fundamental winding factors can be used as a guideline for selecting machines as it plays a crucial role in torque production and machine efficiency [25]. Furthermore, low harmonic winding factors are desired, especially w.r.t. the fifth and seventh harmonic, to prevent waveform distortion and additional losses. Fundamental winding factors for different combinations of slots, N_s , and poles, P , are shown in Fig. 4.2 [25]. The maximum electrical frequency of the motor is usually constrained to approximately 400 Hz to ensure a good efficiency at high speed. The conditions of symmetry that govern whether a winding layout is symmetrical or not must also be known. This ensures windings fed from a symmetrical three-phase supply produce a rotating magnetic field [19]. While integral slot windings are always symmetrical, fractional-slot windings must adhere to symmetry conditions. For a given $q = \frac{z}{n}$, as defined in Eq. 4.3, where z and n are not mutually divisible, the following conditions apply [19]:

$$q = \frac{Q_s}{2pm} \quad (4.3)$$

Table 4.2: Dimensions and specifications of SPM

Parameter	Value
Outer diameter [D_{out}]	212 mm
Shaft diameter [D_{shaft}]	30 mm
Output power [P_{out}]	3 kW
Maximum voltage [V_{max}]	48 V _{LL}
Phase current [$I_S = I_{lim}$]	44 A
Peak losses [P_{loss}]	300 W
Base speed [$N_{p(base)}$]	1500 rpm
Maximum speed [$N_{p(max)}$]	5000 rpm
Torque at base speed [$T_{p(max)}$]	19.1 rpm
Torque at maximum speed [$T_{p(min)}$]	5.73 rpm
Winding temperature [$T_{winding}$]	120 °C
PM material	NdFeB N48H
PM remnant flux density [B_r]	1.2899 T
PM recoil permeability [μ_r]	1.05
Core material	M19_26G

Table 4.3: Possible winding layouts

p	$n = 2$	$n = 4$	$n = 5$	$n = 7$	$n = 8$
1	D	N	N	N	N
2	B	D	N	N	N
3	D	N	N	N	N
4	B	B	N	N	D
5	D	N	B	N	N

1. First condition:

- For single-layer windings: $\frac{p}{n} \in N$
- For double-layer windings: $\frac{2p}{n} \in N$

2. Second condition: $\frac{n}{3} \notin N$ for three-phase systems.

Based on these symmetry constraints, the possible windings layouts for different combinations of p and n are given in Table 4.3. Note single-layer windings are denoted by S, double-layer windings by D and cases where both single-and double layer windings are possible by B. N indicates no symmetrical winding layout is possible. **Based on winding factors, frequency constraints and literature, the following machines are selected for the design study: 12-slot 10-pole single-layer winding machine, 12-slot 10-pole double-layer winding machine and an 36-slot 8-pole double-layer winding machine.** As shown in Table 4.4, all these machines offer high fundamental winding factors and low harmonic winding factors.

P Ns	2	4	6	8	10	12	14	16	18	20	22
3	0.8660	0.8660		0.8660	0.8660		0.8660	0.8660		0.8660	0.8660
6	1	0.8660		0.8660	0.5000		0.5000	0.8660		0.8660	0.5000
9	0.9452	*0.9452 0.6169	0.8660	0.9452	0.9452	0.8660	0.6169	0.3283		0.3283	0.6169
12	0.9659	1		0.8660	0.9330		0.9330	0.8660		0.5000	0.2500
15	0.9514	0.9099		0.7109	0.8660		0.9514	0.9514		0.8660	0.7109
18	0.9598	0.9452	1	0.9452 0.6169	0.7352	0.8660	0.9019	0.9452		0.9452	0.9019
21	0.9531	0.9531		0.8897 0.5384	0.9531 0.6501		0.8660	0.8897		0.9531	0.9531
24	0.9577	0.9659		1	0.9250 0.5830		0.7598	0.8660		0.9330	0.9495
27	0.9539	0.9410	0.9452	0.9410	0.8773 0.5250	0.9452 0.6169	0.6950	0.7664	0.8660	0.8773	0.9153
30	0.9567	0.9514		0.9099	1		0.9514 0.6401	0.7109		0.8660	0.8740
33	0.9542	0.9542		0.9542	0.9456		0.9284 0.5905	0.9542 0.6592		0.7782	0.8660
36	0.9561	0.9598	0.9659	0.9452	0.9236	1	0.8985 0.5484	0.9452 0.6169		0.7352	0.7832
39	0.9544	0.9482		0.9175	0.8931		0.8630 0.5105	0.9175 0.5738		0.6889	0.7399
42	0.9558	0.9531		0.9531	0.9531		1	0.8897 0.5384		0.9531 0.6501	0.7007

Figure 4.2: Winding factors for different slot(N_s) and pole (P) combinations.

4.3. Winding layouts

To perform winding layouts using coil voltage phasor diagrams (star of slots), some basic parameters have to be defined for the machine [19]. The slot angle in electrical radians, α_u , shown in Eq. 4.4, the coil pitch in number of slots, γ_Q , shown in Eq. 4.5, the number of phases, m , and the machine periodicity, t , given by Eq. 4.7. For fractional-slot windings, γ_Q is not a natural number and thus these will be short-pitched windings, i.e. $\gamma < \gamma_Q$. Note m is the number of phases and that all angles are given in electrical radians, defined in Eq. 4.6, unless specified otherwise. For fractional-slot windings, base-winding phasor diagrams are used which represent the smallest independent symmetrical section of a winding, which can be repeated t times in a machine [19].

$$\alpha_u = \frac{2\pi p}{Q_s} \quad (4.4)$$

$$\gamma_Q = \frac{Q_s}{2p} \quad (4.5)$$

$$\theta_{elec} = p\theta_{mech} \quad (4.6)$$

$$t = GCD\{Q_s, p\} \quad (4.7)$$

With these quantities known, the phasor diagram can be constructed starting with a circle. The circle can be divided into $2m$ sectors each having $\frac{Q_s}{2mt}$ phasors, with two opposite sectors assigned to a phase- one positive and one negative sector. For three-phase windings, phases must be separated by 120 electrical degrees. The phasors are numbered, 1 through Q_s , with α_u the angle between consecutive slots. For cases where t is an odd number, natural zone variation must be employed, meaning positive and negative zones will differ by one phasor. This occurs in some double-layer windings and is compensated by the reverse happening in the second layer of the winding. For double-layer windings, after assigning the top layer according to the phasor diagram, the bottom layer is assigned based on γ [19], [26].

4.3.1. Winding layout: 12-slot 10-pole machine

The phasor diagram of the base winding of both the single-and double-layer winding machine is shown in Fig. 4.4a. Regarding the double-layer winding, $\gamma_Q = 1.2$, so the coil pitch is chosen as $\gamma = 1$. The winding layouts are shown in Fig. 4.3. The winding factors for the 12-slot 10-pole machine are given by Eq. 4.8 for the single-layer case and Eq. 4.9 for the double-layer case, with v the harmonic order [18]. Winding factors are summarised in Table 4.4. Note the third harmonic is neglected as this cancels between phases ($m = 3$) [19].

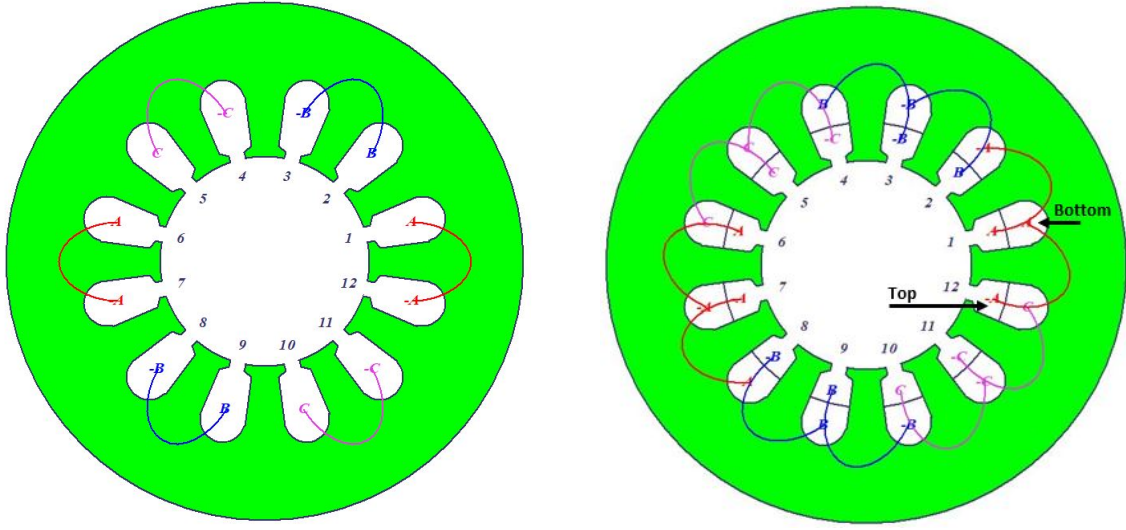
$$k_{wv} = \sin\left(\frac{vp\pi}{Q_s}\right) \quad (4.8)$$

$$k_{wv} = \sin^2\left(\frac{vp\pi}{Q_s}\right) \quad (4.9)$$

4.3.2. Winding layout: 36-slot 8-pole machine

The phasor diagram of the double-layer base winding is shown in Fig. 4.4b. Since $\gamma_Q = 4.5$, the coil pitch is chosen as $\gamma = 4$. The double-layer winding layout is shown in Fig. 4.5. The fundamental winding factor of the 36-slot 8-pole machine is determined using its base winding phasor diagram, with negative coil voltage phasors rotated by 180° (indicated with negative signs in Fig. 4.4c). The line of symmetry is found using vector addition, where after k_{w1} can be found based on Eq. 4.10 with Z , α_ρ the number of phasors and the angle between the ρ^{th} phasor and the line of symmetry respectively. k_{w1} is calculated as shown in Eq. 4.11.

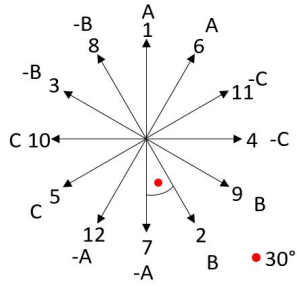
$$k_{wv} = \frac{\sin\left(\frac{v\pi}{2}\right)}{Z} \sum_{\rho}^Z \cos(\alpha_\rho) \quad (4.10)$$



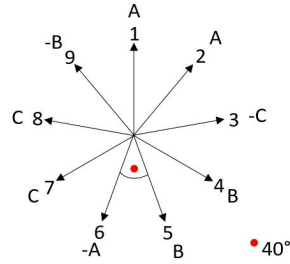
(a) Single-layer 12-slot 10-pole machine

(b) Double-layer 12-slot 10-pole machine

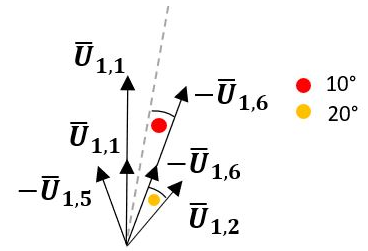
Figure 4.3: Winding layouts for 12-slot 10-pole machine



(a) Base winding: 12s10p



(b) Base winding: 36s8p



(c) K_{w1} calculation: 36s8p

Figure 4.4: Phasor diagrams

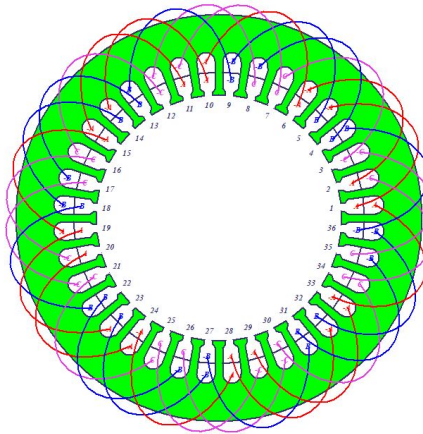


Figure 4.5: Double-layer winding of 36-slot 8-pole machine

Table 4.4: Winding factors

Configuration	$v = 1$	$v = 5$	$v = 7$
12s10p(S)	0.966	0.259	0.259
12s10p(D)	0.933	0.067	0.067
36s8p(D)	0.9452	0.1398	-0.0607

Table 4.5: Current limits for air-cooled PMSMs

	K_s (kA/m)	J (A/mm ²)
Typical value	35-65	3-5

$$k_{w1} = \frac{\sin(\frac{\pi}{2})}{6} (4 \cos(\frac{\pi}{18}) + 2 \cos(\frac{\pi}{6})) \quad (4.11)$$

4.4. Initial sizing of design parameters

The design procedure followed is based on work in [27], [28]. This procedure requires choosing certain parameters, shown in Table 4.6, in addition to those in Table 4.2 before starting the initial design process. Thermal considerations are included through the choice of K_s and J, with guidelines shown in Table 4.5. Magnetic saturation is considered through the choice of $B_{ys(max)}$ and $B_{ts(max)}$ and manufacturing constraints through f_f . Note the initial design procedure is performed using parameters at base speed.

4.4.1. Geometric dimensions

Firstly, the air gap flux is calculated. It is approximated as a square wave with amplitude B_g , given by Eq. 4.12, with a fundamental sinusoidal component B_{g1} , given by Eq. 4.13. Note the Carter factor, K_c , is assumed to be 1.05. A more detailed air-gap flux calculation

Table 4.6: Input parameters for design at 1500 rpm

Parameter	12s10p(S)	12s10p(D)	36s8p(D)
Magnet thickness [h_m]	3 mm	3 mm	2 mm
Slot opening [w_0]	2 mm	2 mm	2 mm
Slot enclosure depth [h_1]	4 mm	4 mm	4 mm
Electrical frequency [f]	125 Hz	125 Hz	100 Hz
Air gap size [g]	1 mm	1 mm	1 mm
Pole coverage ratio [α_p]	0.83	0.83	0.83
$B_{ys(max)}$	1 T	1 T	1 T
$B_{ts(max)}$	1.6 T	1.6 T	1.6 T
Lamination stacking factor [k_j]	0.95	0.95	0.95
Current density [J]	4 A/mm ²	4 A/mm ²	4 A/mm ²
Linear Current density [K_s]	35 kA/m	35 kA/m	35 kA/m
Fill factor [f_f]	35%	35%	35%

method is shown in Appendix C. The air gap diameter, D_{ag} , measured to the middle of the air gap, is calculated from Eq. 4.14. Note that the stack length, L , is related to the air gap diameter as shown in Eq. 4.15, with ψ chosen as 1. With the external rotor diameter, $D_{er} = D_{ag} - 2h_m - g$, and the internal stator diameter, $D_{is} = D_{ag} + g$, the pole pitch and slot pitch can be calculated from Eq. 4.16 and Eq. 4.17 respectively.

$$B_g = B_r \frac{\frac{h_m}{\mu_r}}{\frac{h_m}{\mu_r} + gK_c} \quad (4.12)$$

$$B_{g1} = \frac{4}{\pi} B_g \sin\left(\frac{\alpha_p \pi}{2}\right) \quad (4.13)$$

$$T_r = \frac{\sqrt{2}\pi}{4} B_{g1} K_s D_{ag}^2 L \quad (4.14)$$

$$\psi = \frac{L}{D_{ag}} \quad (4.15)$$

$$\tau_p = \frac{\pi D_{is}}{2p} \quad (4.16)$$

$$\tau_s = \frac{\pi D_{is}}{Q_s} \quad (4.17)$$

The stator yoke thickness, h_{ys} , and tooth width, w_{tt} , can be calculated from Equations 4.18 and 4.20 respectively. Note that in the case of FSCW machines where the magnet circumference is comparable to the slot pitch, Equations 4.19 and 4.21 must be used to account for the flux shunting effect between two adjacent magnets [27].

$$h_{ys} = \frac{B_g \alpha_p \tau_p}{2B_{ys(max)} k_j} \quad (4.18)$$

$$h_{ys} = \frac{B_g}{B_{ys(max)} k_j} \left(\alpha_p \tau_p - \frac{\tau_s - \tau_p}{2} \right) \quad (4.19)$$

$$w_{tt} = \frac{B_g \tau_s}{B_{ts(max)} k_j} \quad (4.20)$$

$$w_{tt} = \frac{B_g}{B_{ts(max)} k_j} \left(\alpha_p \tau_p - \frac{\tau_s - \tau_p}{2} \right) \quad (4.21)$$

To determine further slot dimensions as shown in Fig. 4.6, D_{h1} is defined as shown in Eq. 4.22 with slot enclosure dimensions, h_{11} and h_{12} , chosen as 2 mm each to sum to h_1 . The slot width, w_{st} , measured at the same diameter as w_{tt} is calculated as shown in Eq. 4.23.

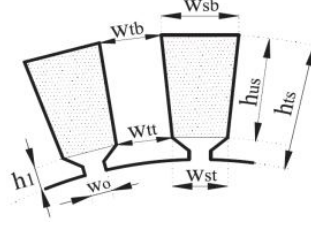


Figure 4.6: Slot dimensions as used for initial geometric sizing

$$D_{h1} = D_{is} + 2h_1 \quad (4.22)$$

$$w_{st} = \frac{\pi D_{h1}}{Q_s} - w_{tt} \quad (4.23)$$

The required stator slot area is calculated from Eq. 4.24, which excludes the slot enclosure area. Lastly the stator slot height, h_{us} which excludes the slot enclosure dimensions, can be calculated from Eq. 4.27. The slot area is approximated as a trapezoid, as shown in Eq. 4.25, to make initial sizing calculations easier. The outer slot width, w_{sb} , is given by Eq. 4.26. Note the tooth width is constant due to the trapezoidal slot shape. The outer stator diameter is given by Eq. 4.28.

$$A_{us} = \frac{\pi D_{h1} K_s}{J Q_s K_{w1} f_f} \quad (4.24)$$

$$A_{us} = \left(\frac{w_{st} + w_{sb}}{2} \right) h_{us} \quad (4.25)$$

$$w_{sb} = \left(\frac{\pi (D_{h1} + 2h_{us})}{Q_s} \right) - w_{tt} \quad (4.26)$$

$$h_{us} = \frac{-w_{st} + \sqrt{w_{st}^2 + \left(\frac{4\pi A_{us}}{Q_s} \right)}}{\frac{2\pi}{Q_s}} \quad (4.27)$$

$$D_{out} = D_{h1} + 2(h_{us} + h_{ys}) \quad (4.28)$$

4.4.2. Calculation of number of turns per phase

The number of turns per phase can be calculated according to Eq. 4.29, with α_p used for PM machines where the magnet thickness is constant [19]. Note that the back-EMF, E_m , is assumed equal to the line-to-neutral phase voltage value, $L' = L + 2g$ and ω_e is the electrical frequency in rad/s. The number of turns must be chosen which allows for an integer number of conductors, z_Q , per slot, or per half slot for a double layer winding

Table 4.7: Initial geometric parameters

Parameter	12s10p(S)	12s10p(D)	36s8p(D)
Slot opening depth [h_{11}]	2 mm	2 mm	2 mm
Slot height [h_{slot}]	35.3 mm	36.08 mm	32.95 mm
Slot area [A_{us}]	568.87 mm ²	588.99 mm ²	201.22 mm ²
Air gap diameter [D_{ag}]	74.96 mm	74.96 mm	78.18 mm
Stack Length [L]	74.96 mm	74.96 mm	78.18 mm
Stator yoke thickness [h_{ys}]	21.79 mm	21.79 mm	11.37 mm
Rotor yoke thickness [h_{yr}]	18.98 mm	18.98 mm	21.59 mm
Tooth width [w_{tt}]	13.62 mm	13.62 mm	3.81 mm
Slot width [w_{st}]	8.36 mm	8.36 mm	3.8 mm
Outer diameter [D_{out}]	194.15 mm	195.7 mm	171.82 mm
Turns per phase [N_{ph}]	30	32	36
Turns per coil [N_{coil}]	15	8	3

layout. The condition for a single layer winding is given in Eq. 4.30 and in Eq. 4.31 for a double layer winding.

$$N_{ph} = \frac{\sqrt{2}E_m}{\omega_e K_{w1} \alpha_p B_{g1} \tau_p L'} \quad (4.29)$$

$$z_Q = \frac{N_{ph}}{pq} \quad (4.30)$$

$$z_{Q(half-slot)} = \frac{N_{ph}}{2pq} \quad (4.31)$$

Flux density in the rotor is calculated to ensure no saturation occurs, based on Eq. 4.32 and Eq. 4.33. Parameters obtained from the initial design process is shown in Table 4.7. Note $h_{slot} = h_{us} + h_{12}$ and $h_{yr} = \frac{D_{er} - D_{shaft}}{2}$.

$$\phi_{rot} = B_g \alpha_p \tau_p L \quad (4.32)$$

$$B_{yr} = \frac{\frac{\phi_{rot}}{2}}{\frac{(D_{er} - D_{shaft})}{2} L k_j} \quad (4.33)$$

4.5. Additional considerations for final design

4.5.1. Cogging torque and torque ripple

Cogging torque is produced by the interaction of MMF harmonics produced by the PM's and air gap permeance harmonics due to the effects of stator slotting. It causes the rotor to tend to align in stable positions which can cause speed ripples and vibration [29]. For the purposes of this report, three aspects which influence cogging torque are investigated: slot

Table 4.8: Cogging torque parameters

Parameter	12s10p(S)	12s10p(D)	36s8p(D)
N_C	60	60	72
C_T	2	2	4
$\alpha_{p(opt)}$	0.8433	0.8433	0.8989

and pole combinations, slot opening width and magnet pole coverage ratio (α_p). From [29], the factor C_T is introduced as a measure of the cogging torque produced by a certain pole-slot combination, as shown in Eq. 4.34. A larger C_T value is related to a larger cogging torque [29]. N_C is the smallest common multiple of Q_s and $2p$. The optimal magnet pole coverage ratio is given by Eq. 4.35, taking magnet fringing into account through k_2 , which typically ranges between 0.01 and 0.03. k_1 is chosen as 1 to maximise the air gap flux [29]. Note $N = \frac{N_C}{2p}$. These quantities are shown in Table 4.8 for the machines investigated, with $k_2 = 0.01$. Regarding slot openings, the cogging torque must be considered under both open-circuit and full-load conditions. Under open-circuit conditions, the amplitude of the cogging torque decreases as the slot opening width decreases. The same phenomenon is observed under full-load conditions as the stator slotting effect decreases which reduces the variation of the air gap permeance. However, this is only valid until a certain point where after the cogging torque amplitude increases again as the tooth-tip leakage flux enhances local magnetic saturation which causes the air gap permeance variation to increase once again [30]. Accordingly, an optimal point exists for the slot opening width to decrease the cogging torque. It should be kept in mind that due to saturation effects, the optimal design for reducing cogging torque might not result in the minimum torque ripple [30].

$$C_T = \frac{2pQ_s}{N_C} \quad (4.34)$$

$$\alpha_{p(opt)} = \frac{N - k_1}{N} + k_2 \quad (4.35)$$

4.5.2. Demagnetization aspects

A typical demagnetization curve, which refers to the second quadrant of the BH-curve, is shown in Fig. 4.7a. The magnet originally has a remnant value, B_R . As a negative MMF, i.e. current, is applied to the stator windings, the B-H curve will be traced towards (a). If the MMF is then increased to zero again, the minor hysteresis loop is traced to (b). This minor hysteresis loop is approximated by a straight line of which the slope is the recoil permeability, μ_R . From Fig. 4.7a, if a small negative current is applied so that only point (d) is reached, the magnet traces the recoil line back to (c) with almost no loss of residual magnetization. If a large negative current is applied that goes beyond (a), also known as the knee point, there is a significant reduction in residual magnetism,

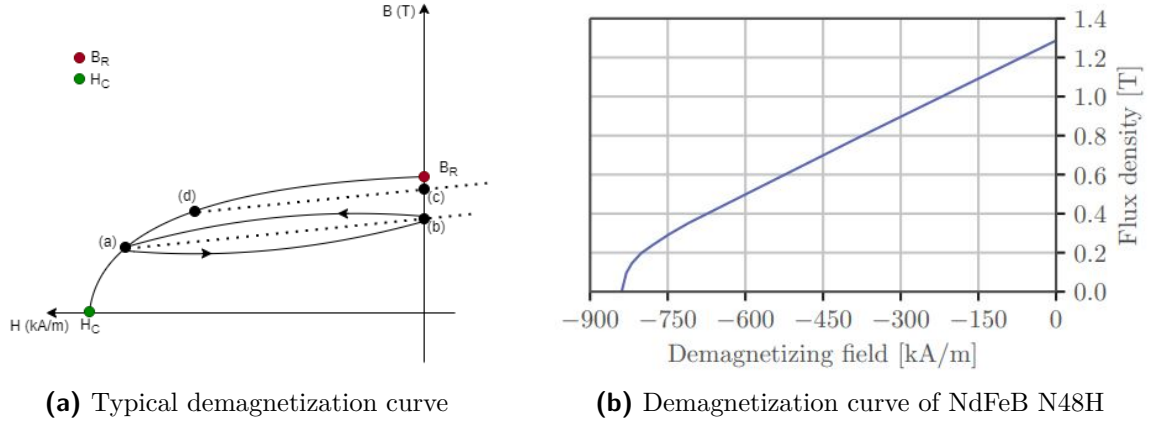


Figure 4.7: Demagnetization characteristics

referred to as demagnetization. The demagnetization curve of NdFeB N48H is shown in Fig. 4.7b. When machine design is considered, the concept of a demagnetization margin is introduced which refers to how far above the knee point the machine operates. The knee point of NdFeB N48H occurs at 0.2 T.

4.6. Optimum design of PM motors

The aim of any design optimisation can be summarised as follows: find a vector \mathbf{X} , that represents a set of n design variables, each bounded by $x_{il} \leq x_i \leq x_{ih}$ with $i = 1, \dots, n$ to minimise an objective function $F(\mathbf{X})$ and satisfy a set of m constraints, $G_k(\mathbf{X}) \leq 0$ with $k = 1, \dots, m$ [31]. For the design of a fractional-slot machine, the vector \mathbf{X} will contain physical machine dimensions and constraints such as the torque and losses. Traditionally, this optimisation problem has been solved using gradient based methods [32], [33]. Modern approaches have also been developed, such as genetic algorithms and particle swarm optimisation [33], [34], [35] and these have been implemented in design procedures [36], [37].

4.6.1. Formulation of optimisation problem

The optimisation strategy employed will analyse the two critical points at base and maximum speed, as shown in Fig. 3.5b, using FEA. By analysing the designs at $N_{p(base)}$, a constant torque speed range (CTSR) is ensured. Note $N_{p(init)} = 1$ rpm. By analysing the designs at $N_{p(base)}$ and $N_{p(max)}$, a constant power speed range (CPSR) is ensured. Adopting the strategy proposed in [13], the optimisation problem is formulated as in [13], shown below Fig. 4.8. Note that all values are RMS values and the voltage is a line-to-line quantity. \mathbf{X} is a vector containing design variables including the dq-currents, geometric variables and coil turns [13].

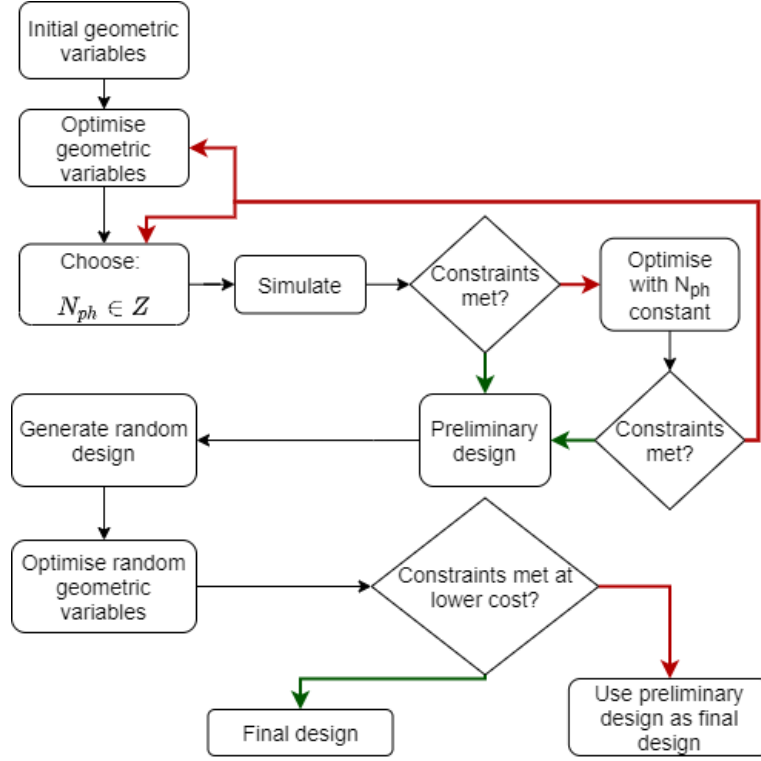


Figure 4.8: Optimisation process

Minimise: $F(\mathbf{X}) = C_{total}$

Subject to: $T_1 \geq 19.1 \text{ Nm}$ $T_2 \geq 5.73 \text{ Nm}$

$V_{max1} \leq 48 \text{ V}$ $V_{max2} \leq 48 \text{ V}$

$I_{S1} \leq 42.5 \text{ A}$ $I_{S2} \leq 42.5 \text{ A}$

$P_{loss1} \leq 265 \text{ W}$ $P_{loss2} \leq 265 \text{ W}$

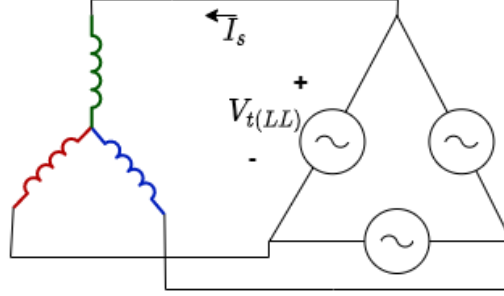
$B_{MM1} \geq 0.05 \text{ T}$ $B_{MM2} \geq 0.05 \text{ T}$

4.6.2. Finite element based optimisation process

The optimisation process was implemented in SEMFEM, an 2D finite element package. The process followed is shown in Fig. 4.8, starting with the optimisation of initial geometric variables. The number of turns per phase must then be chosen to be a valid, integer number as the optimisation may result in non-integer N_{ph} values. Should the choice still satisfy constraints, a preliminary design is found. Alternatively, the dimensions are optimised again with N_{ph} constant to check if constraints can be satisfied. If no valid design is found, the whole process is restarted changing either the choice of N_{ph} or the boundaries. To ensure, within computational limits, that a global optimum is found, random variable sets are generated and optimised. Should all constraints be met at a lower price, this design becomes the final design. Note that optimisations are performed with a coarser mesh compared to simulations due to time constraints.

Table 4.9: dq-current densities of machines

Parameter	12s10p(S)		12s10p(D)		36s8p(D)	
	1500 rpm	5000 rpm	1500 rpm	5000 rpm	1500 rpm	5000 rpm
$i_{q(dens)}$ (A/mm ²)	3.845	1.153	3.961	1.188	4.348	1.304
$i_{d(dens)}$ (A/mm ²)	-2.392	-4.379	-2.464	-4.511	-2.705	-4.952

**Figure 4.9:** Delta-wye connection of motor

4.6.3. Finite element based simulation methods

The solution method used in SEMFEM requires dq-current densities to be specified. Using Eq. 3.18 and 3.17, i_q can be obtained. The d-axis current is then given by $i_d = \sqrt{2}I_s \sin\beta_T$, as explained in Section 3.2. The estimated dq-current densities for the three machines at base and maximum speeds are shown in Table 4.9, calculated using Eq. 4.36 and Eq. 4.37. It should be noted that the dq-currents required are the same for all 3 machines under ideal assumptions. These current densities provide a starting point for the optimisation process. Analysis of the final machines was carried out in ANSYS Maxwell, where the machine is driven by the circuit shown in Fig. 4.9, with the apparent power delivered to the machine given by Eq. 4.38.

$$i_{q(dens)} = \frac{i_q z_Q}{f_f A_{us}} \quad (4.36)$$

$$i_{d(dens)} = \frac{i_d z_Q}{f_f A_{us}} \quad (4.37)$$

$$S_{3\phi} = \sqrt{3}V_{t(LL)}I_s \quad (4.38)$$

Chapter 5

Comparative study of two SPM motors

5.1. Dimensions, inductance and cost

The preliminary machine dimensions found through the optimisation process are shown in Table 5.2. The final machine dimensions are also shown. Changes can be attributed to practical considerations, notably the slot fill factor and wire size selection. With reference to the slot dimensions as shown in Table 5.3 and defined as shown in Fig. 5.1, the preliminary slot dimensions were adjusted for two reasons. The first is to achieve a slot fill factor of near 35%, which is achievable if the machines are manufactured in-house. This slot fill factor must be achieved using standard wire sizes, and thus each conductor consists of z_{wire} wires. The second reason is to decrease L_s , to ensure a better power factor as the original machine delivered a poor power factor when analysed in ANSYS Maxwell. The inductance values of the final machines are shown in Table 5.1. As stated in Chapter 3, it is clear that the harmonic leakage inductance contributes significantly towards L_s in the case of the FSCW machines, while L_m contributes significantly in the FSDW machine case. This can be attributed to the higher harmonic content of the concentrated windings due to a less sinusoidal winding distribution. For both FSCW and the FSDW machine, the slot leakage inductance is the dominant component. This is thought to be the result of the optimisation process, which seeks to maximise this quantity. The costs and mass of the final machines are shown in Table 5.4. The 12-slot double-layer machine uses the least amount of all materials and thus has the lowest cost. This is due to short end windings which reduce copper usage, a small diameter which reduces steel consumption and thinner magnets, which greatly reduce costs.

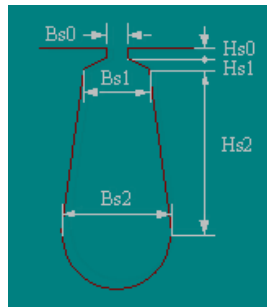


Figure 5.1: Slot dimensions

Table 5.1: Inductances of machines

Inductance	12s10p(S)	12s10p(D)	36s8p(D)
L_σ (μH)	586.3	430.67	606.8
L_{ew} (μH)	2.61	1.36	52.74
L_h (μH)	178.34	115.79	7.97
L_m (μH)	68.95	152.6	344.78
L_s (μH)	836.2	700.43	1012.3
R_{DC} ($m\Omega$ @ 20 °C)	22.254	21.91	33.678

Table 5.2: Main machine dimensions

Parameter	12s10p(S)		12s10p(D)		36s8p(D)	
	Preliminary	Final	Preliminary	Final	Preliminary	Final
D_{shaft} (mm)	30	30	30	30	30	30
h_{yr} (mm)	10.984	10.984	18.3	18.3	21.075	20.575
h_m (mm)	4.754	4.754	2.32	2.32	2	2.5
α_p	0.75	0.75	0.7577	0.7577	0.7258	0.7258
g (mm)	1	1	1	1	1	1
h_{ys} (mm)	9.162	10.628	4.555	3.798	5.243	5.188
D_{out} (mm)	170.142	170.142	156.755	156.755	184.92	184.92
L (mm)	108.673	108.673	95.825	95.825	70.21	70.21
N_{coil}	20	20	11	11	5	5
N_{ph}	40	40	44	44	60	60

Table 5.3: Slot parameters

Parameter	12s10p(S)		12s10p(D)		36s8p(D)	
	Preliminary	Final	Preliminary	Final	Preliminary	Final
h_{s0} (mm)	3.272	3.272	5.756	4	5.128	5.187
h_{s1} (mm)	0	0	0	0	0	0
h_{s2} (mm)	30.639	26	20.205	22	38.243	38.243
b_{s0} (mm)	4.187	4.187	3.326	3.326	1.8	1.6
b_{s1} (mm)	5.125	6.2	12.64	14	3.324	5
b_{s2} (mm)	20.52	27	22.485	24	9.555	9.555
d_{wire} (mm)	3.582	1.628	3.399	1.45	3.61	1.45
z_{wire}	1	4	1	5	1	5
f_f (%)	35	38.05	35	38.2	35	37.3

Table 5.4: Cost and mass of final machines

Material	12s10p(S)		12s10p(D)		36s8p(D)	
	Mass (kg)	Cost (\$)	Mass (kg)	Cost (\$)	Mass (kg)	Cost (\$)
Copper	2.31	15.41	2.234	14.90	3.434	22.90
Magnets	0.518	25.90	0.273	13.65	0.221	11.05
Steel	9.64	19.28	6.943	13.89	7.002	14.00
Total	12.468	60.59	9.45	42.44	10.657	47.95

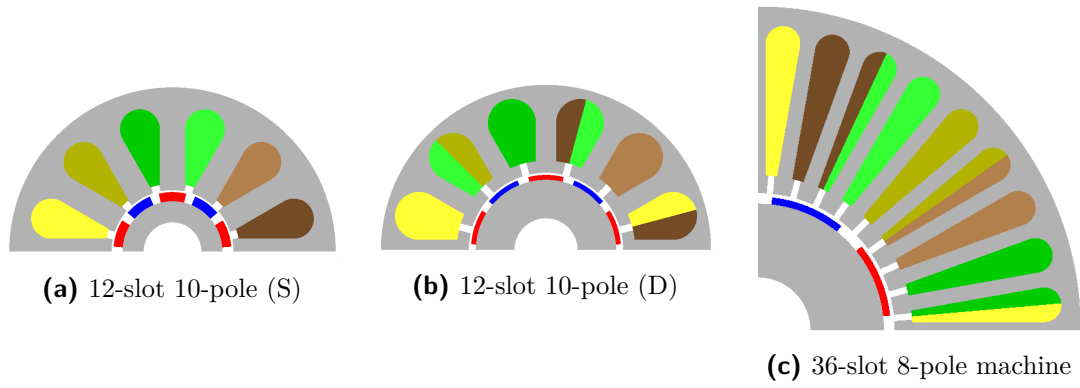


Figure 5.2: Preliminary optimised machines

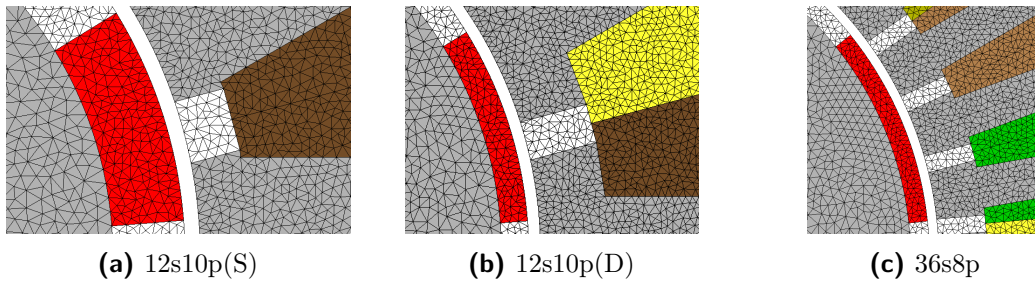


Figure 5.3: Mesh used in SEMFEM

5.2. Main performance characteristics

The main performance aspects of the preliminary and final machines are shown in Tables 5.5 and 5.6 at 1500 rpm and 5000 rpm respectively. Note that preliminary results were obtained using the SEMFEM package while final results were obtained through ANSYS Maxwell. Results compare favourably, with difference attributed to slight dimension changes and different solution methods. The meshes used for the various machines are shown in Fig. 5.3 and 5.4 for SEMFEM and Maxwell respectively. Regarding the notation used in figure legends, the number of slots is indicated followed by a letter indicating a single (S) or double (D) layer winding. The subscript indicates whether the result relates to a preliminary (P) or final (F) design.

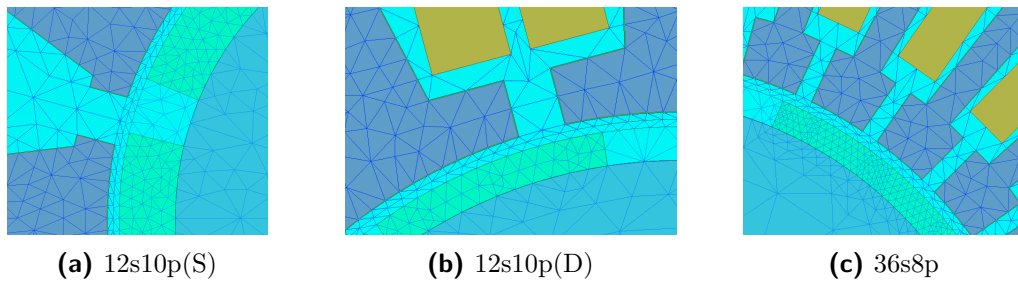
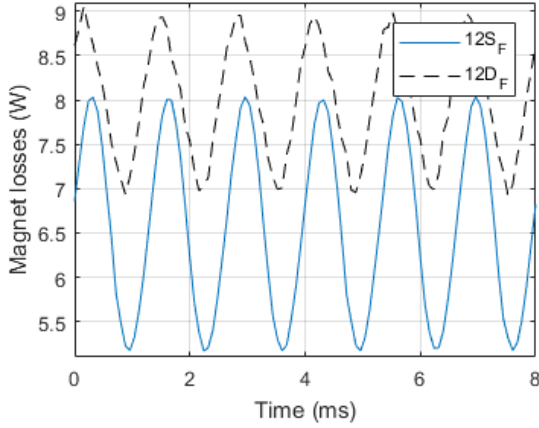
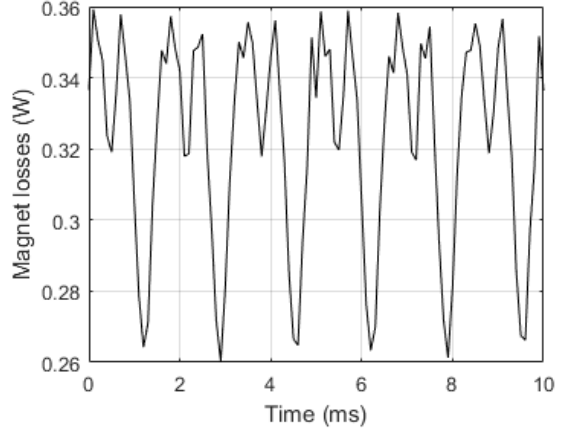


Figure 5.4: Mesh used in ANSYS Maxwell

Table 5.5: Results at 1500 rpm

Parameter	12s10p(S)		12s10p(D)		36s8p(D)	
	Preliminary	Final	Preliminary	Final	Preliminary	Final
T_p (Nm)	19.18	18.43	19.14	19.21	19.379	19.43
T_{rip} (%)	3.36	1.94	6.125	4.49	7.184	6.23
P_{out} (kW)	3.012	2.895	3.043	3.017	3.043	3.053
P_{Cu} (W)	198.1	175.1	211.64	166.94	217.37	251.28
P_{Core} (W)	33.06	31.3	39.95	33.02	42.675	30.48
P_{magnet} (W)	-	6.57	-	7.995	-	0.324
P_{in} (kW)	3.243	3.076	3.264	3.192	3.303	3.335
η (%)	92.87	93.15	92.29	94.53	92.13	92.4
Power factor	0.9285	0.8522	0.9332	0.8988	0.9439	0.94
$V_{t(LL)}$ (V)	47.933	48	48.52	48	48.594	48
$I_{s(RMS)}$ (A)	43.006	43.41	42.66	42.71	42.765	42.27
e_{RMS} (V)	26.223	26.95	26.434	26.78	26.413	25.37
$\lambda_{a(RMS)}$ (mWb)	33.388	33.8	33.657	33.8	42.037	40.4
B_{MM} (T)	0.3072	-	0.3052	-	0.1462	-

**(a)** 12-slot machines**(b)** 36-slot machine**Figure 5.5:** Magnet losses at 1500 rpm

5.2.1. Losses and efficiency

From Tables 5.5 and 5.6, a clear difference between copper and core losses of the preliminary and final designs can be seen. This is due to different end winding lengths in the different software packages, changes to dimensions, different wire sizes and a different core loss calculation method. The 36-slot machine features the highest copper losses at both 1500 and 5000 rpm due to longer end windings, while it has the lowest core losses at 1500 rpm. The 12-slot double-layer winding machine has the highest core losses at 1500 rpm, while at 5000 rpm, the 12-slot single-layer winding machine has the highest core losses. Magnet losses could only be calculated for the final designs using ANSYS Maxwell, and are shown in Fig. 5.5 and 5.6 at 1500 rpm and 5000 rpm respectively. Taking all losses into account, the 12-slot double-layer winding machine has the greatest efficiency at 1500 rpm while the 12-slot single-layer winding machine has the greatest efficiency at 5000 rpm.

Table 5.6: Results at 5000 rpm

Parameter	12s10p(S)		12s10p(D)		36s8p(D)	
	Preliminary	Final	Preliminary	Final	Preliminary	Final
T_p (Nm)	5.766	5.779	5.748	5.8255	5.826	5.75
T_{rip} (%)	11.025	5.77	22.2	11.27	15	11.82
P_{out} (kW)	3.019	3.026	3.015	3.05	3.05	3.01
P_{Cu} (W)	179.2	138.67	202.3	151.72	212.55	248.93
P_{Core} (W)	85.4	79.66	61.61	56.24	53.02	57.09
P_{magnet} (W)	-	51.04	-	55.84	-	2.08
P_{in} (kW)	3.283	3.208	3.279	3.252	3.315	3.252
η (%)	91.94	94.3	91.95	93.79	91.99	92.57
Power factor	0.9863	0.999	0.9872	0.96	0.9686	0.9298
$V_{t(LL)}$ (V)	47.157	48	46.647	48	47.843	48
$I_{s(RMS)}$ (A)	43.06	38.62	42.743	40.72	42.763	42.065
e_{RMS} (V)	25.75	27.1	25.286	27.19	25.95	28.69
$\lambda_{a(RMS)}$ (mWb)	9.836	10.17	9.659	10.23	12.39	13.5
B_{MM} (T)	0.2761	-	0.2933	-	0.224	-

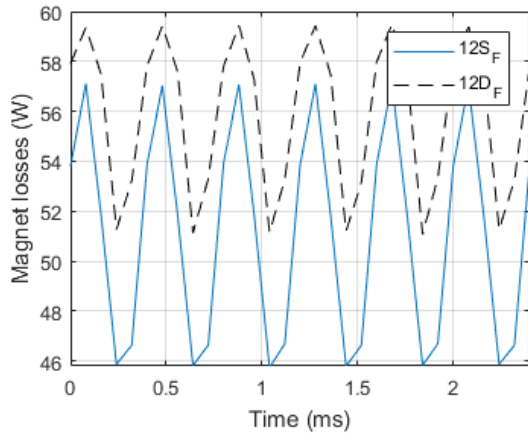
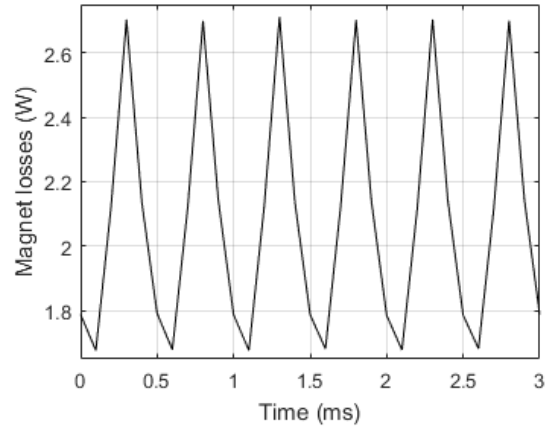
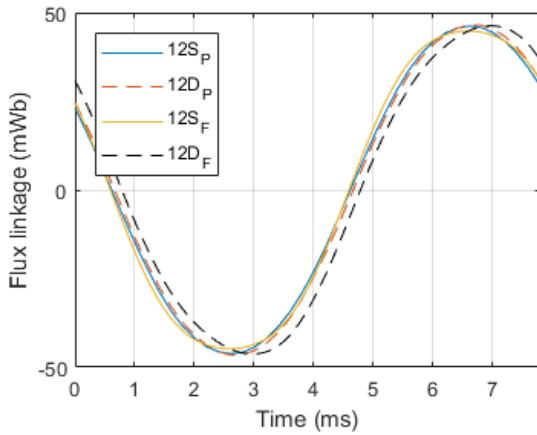
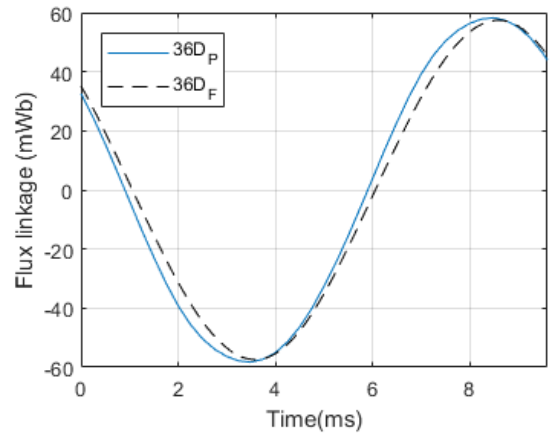
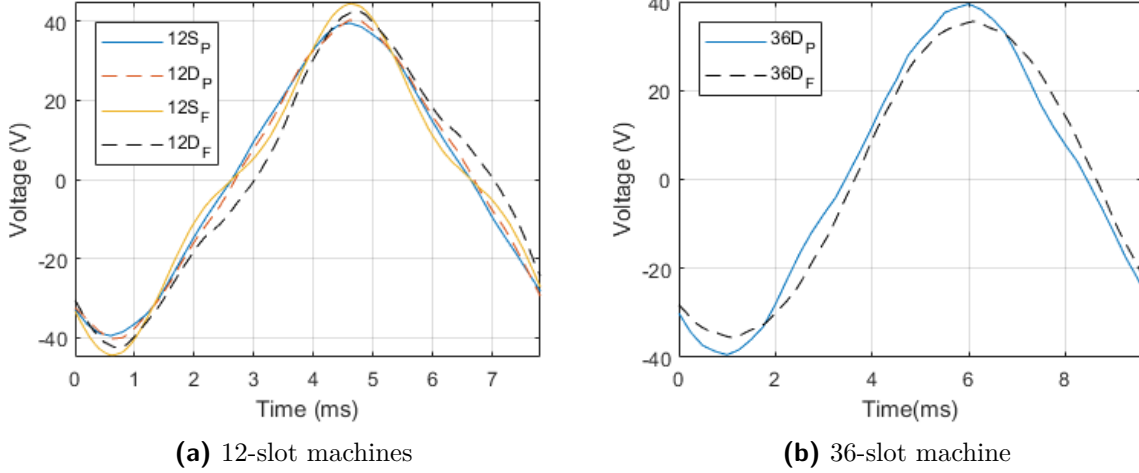
**(a)** 12-slot machines**(b)** 36-slot machine**Figure 5.6:** Magnet losses at 5000 rpm**(a)** 12-slot machines**(b)** 36-slot machine**Figure 5.7:** Flux linkage at 1500 rpm

Table 5.7: Phase angle of terminal voltages

	12s10p(S)		12s10p(D)		36s8p(D)	
	1500 rpm	5000 rpm	1500 rpm	5000 rpm	1500 rpm	5000 rpm
θ_{deg} ($^\circ$)	62	71	52	58	53.2505	55
f_e (Hz)	125	416.67	125	416.67	100	333.33

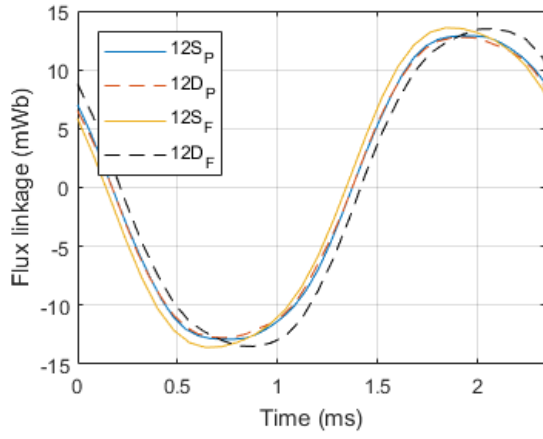
**Figure 5.8:** Induced voltage (back-emf) at 1500 rpm

5.2.2. Flux linkage, voltage and current

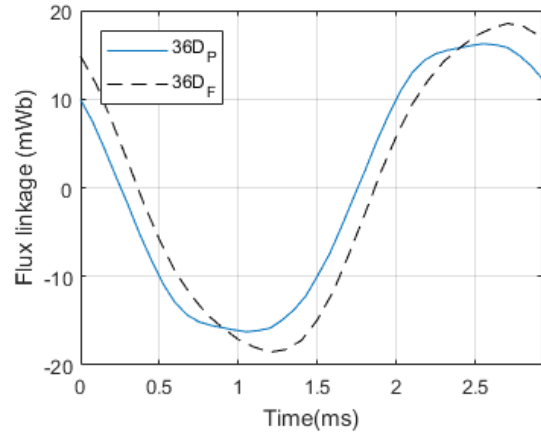
The flux linkage and induced voltages at 1500 rpm are shown in Fig. 5.7 and 5.8. The 36-slot machine produces the most sinusoidal waveform, resulting in a sinusoidal back-emf. Due to flattening at the top of the flux linkage waveforms of the 12-slot machines, distortion occurs around the zero-crossings of the back-emf waveforms. The flux linkage and induced voltages at 5000 rpm are shown in Fig. 5.9 and 5.10. Significant flattening now occurs for all machines, and distorted back-emf waveforms are obtained. In general, higher induced voltages (RMS) are obtained for the final designs. While sinusoidal currents are specified for the simulation of preliminary designs, sinusoidal currents which correlate well are drawn when the simulation is performed using voltage sources, as shown in Fig. 5.11 and 5.12. The power factor, calculated using Eq. 4.38, of the final designs was found to be lower than that of the preliminary designs, with the exception of the 12-slot single-layer machine at 5000 rpm. The input voltages are all of the form shown in Eq. 5.1, with phase angles as shown in Table 5.7 and ω_e as defined in Eq. 5.2. Note these are line-to-neutral quantities and that the phase angle is the torque angle, as described in Chapter 3.

$$v_{an} = 39.1918 \sin(\omega_e t + \theta_{deg} * \frac{\pi}{180}) \quad (5.1)$$

$$\omega_e = \frac{\pi}{30} p N_p \quad (5.2)$$

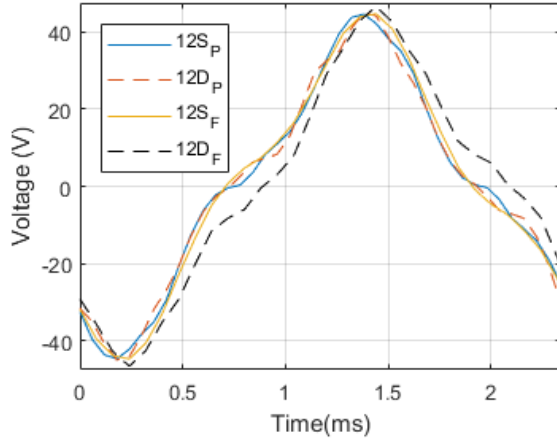


(a) 12-slot machines

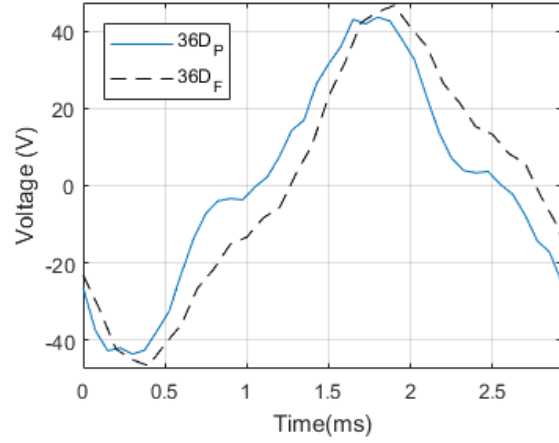


(b) 36-slot machine

Figure 5.9: Flux linkage at 5000 rpm

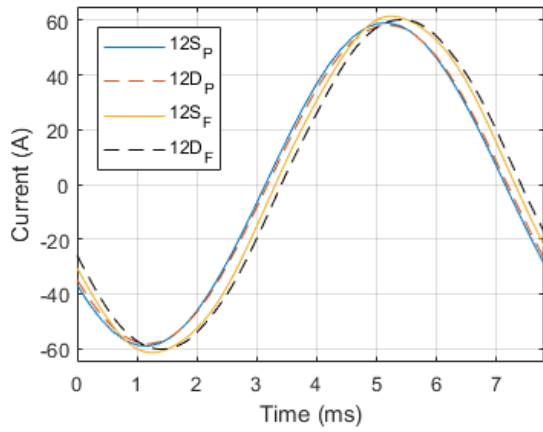


(a) 12-slot machines

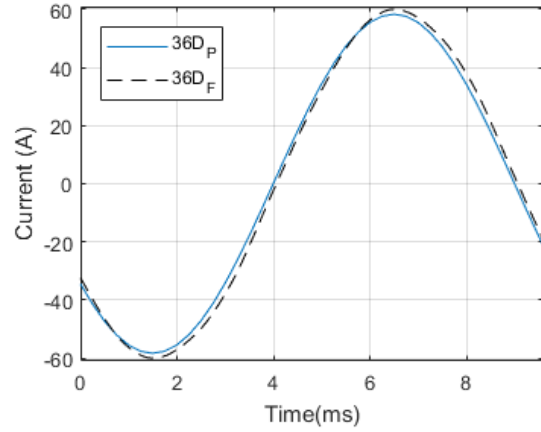


(b) 36-slot machine

Figure 5.10: Induced voltage (back-emf) at 5000 rpm

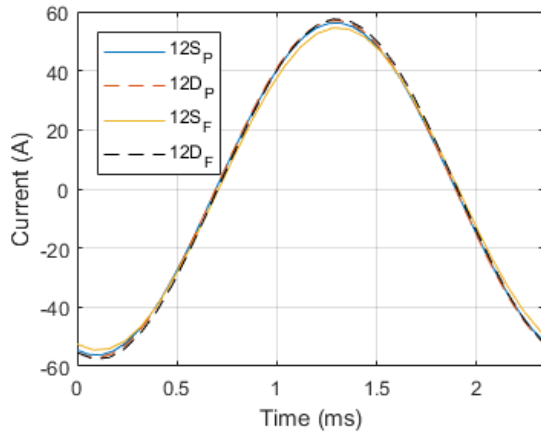


(a) 12-slot machines

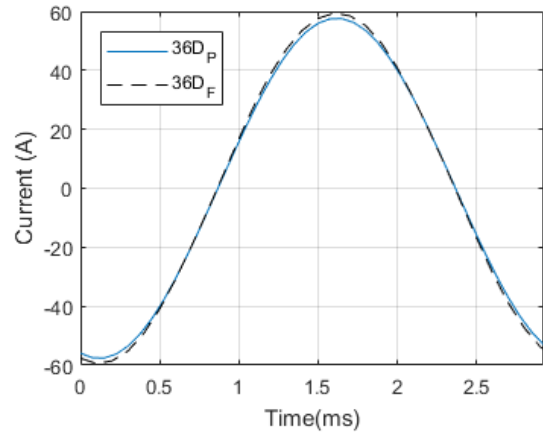


(b) 36-slot machine

Figure 5.11: Phase current at 1500 rpm

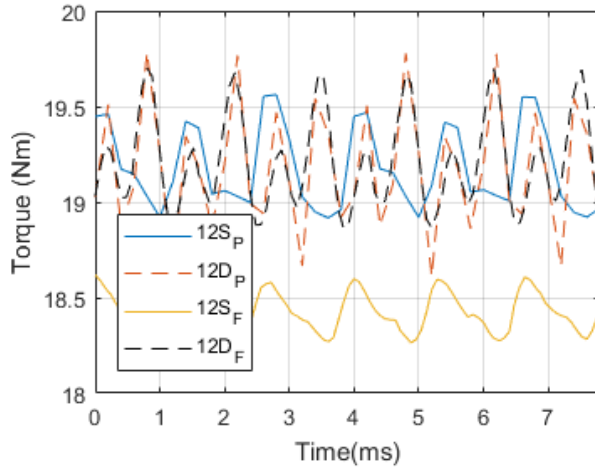


(a) 12-slot machines

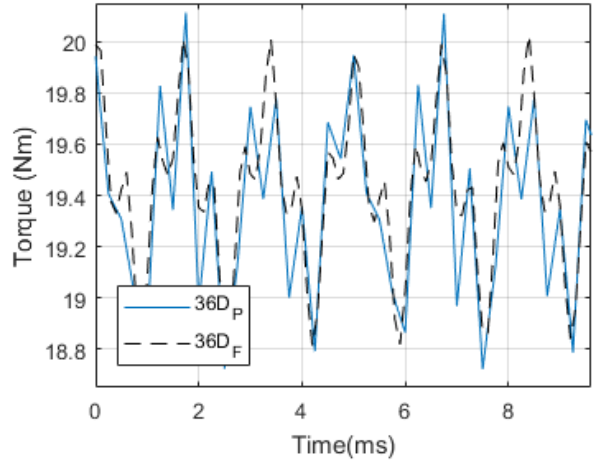


(b) 36-slot machine

Figure 5.12: Phase current at 5000 rpm

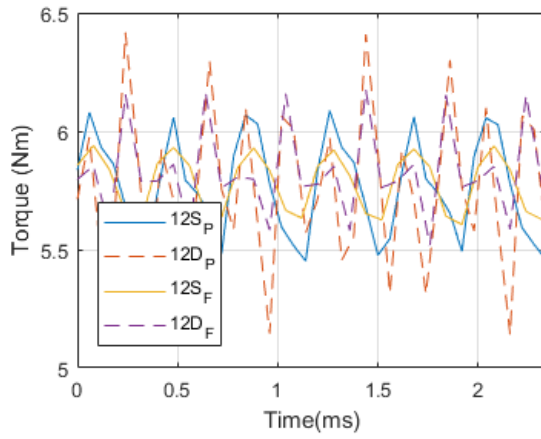


(a) 12-slot machines

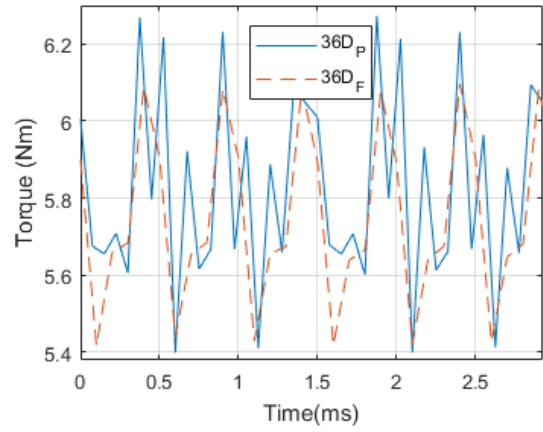


(b) 36-slot machine

Figure 5.13: Output torque at 1500 rpm



(a) 12-slot machines

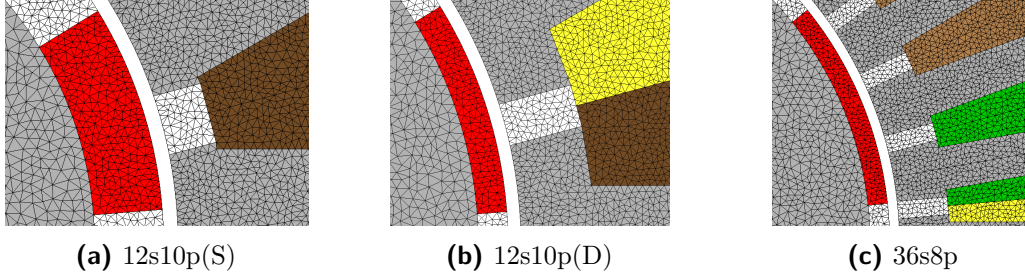


(b) 36-slot machine

Figure 5.14: Output torque at 5000 rpm

Table 5.8: Cogging torque of different machines

Cogging torque	12s10p(S)	12s10p(D)	36s8p(D)
Peak-to-peak (Nm)	0.1672	0.8448	0.7976

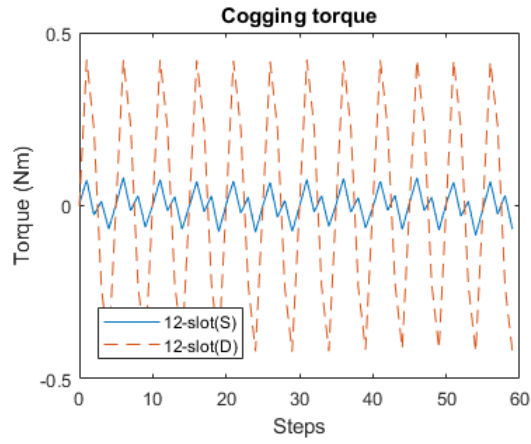
**Figure 5.15:** Mesh used for cogging torque determination

5.2.3. Output torque, torque ripple and cogging torque

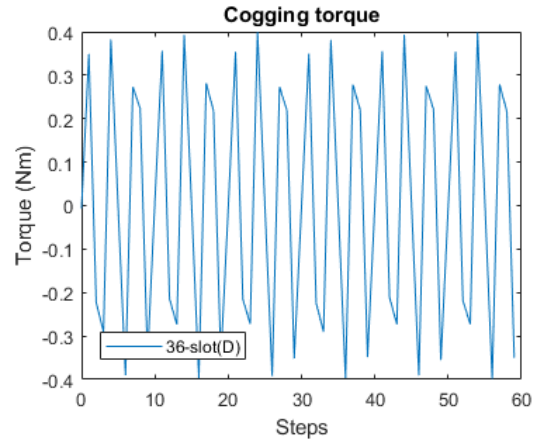
The output torque waveforms are shown in Fig. 5.13 and 5.14 at 1500 rpm and 5000 rpm respectively, with preliminary and final results comparing favourably. The average torque obtained, shown in Tables 5.5 and 5.6, meets traction requirements with the exception of the 12-slot single-layer machine at 1500 rpm. The cogging torque wave forms are shown in Fig. 5.16 for the three preliminary designs, with the maximum and minimum values shown in Table 5.8. The 12-slot single-layer machine has the lowest cogging torque, correlating well with the discussion from Section 4.5.1. The discussion does not correlate well with the obtained result for the other two machines, with the 36-slot machine providing a lower cogging torque than the double-layer 12-slot machine. This shows that while the factor C_T gives an estimation of cogging torque performance, it is not the only aspect to be considered. It is known to accurately determine the cogging torque, a very fine mesh is needed if FEA is used [29]. The mesh used for the three machines is shown in Fig. 5.15. The torque ripple, calculated as a percentage of the average torque, is shown in Tables 5.5 and 5.6. The final design results feature lower torque ripple values, attributed to different solvers and mesh discretisation, with the 12-slot single-layer machine performing best.

5.2.4. Demagnetisation and flux densities

The demagnetisation margins of the preliminary designs are shown in Tables 5.5 and 5.6. The 12-slot machines feature bigger margins due to weaker fields produced by stator windings. In-depth demagnetisation analysis was not performed on the final designs. Flux densities of the 12-slot machines at 1500 rpm are shown in Fig. 5.17 while flux densities of the 36-slot machine at 1500 and 5000 rpm are shown in Fig. 5.18, where flux weakening can be observed. Flux densities of the 12-slot machines are shown in Appendix C, along with efficiency and loss maps generated under the assumption that the motor is always operated at maximum torque per ampere (MTPA).

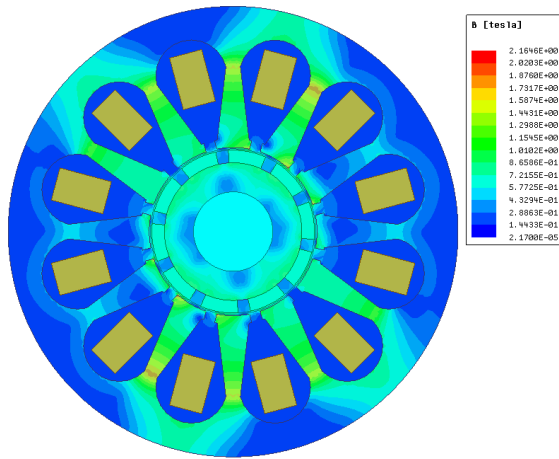


(a) 12-slot 10-pole machine

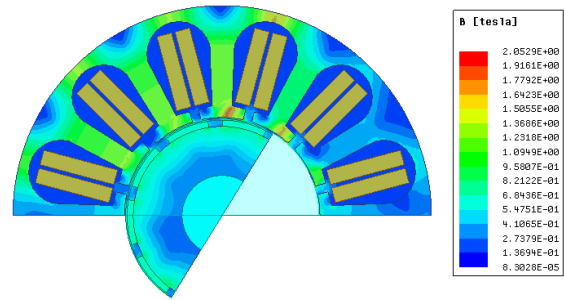


(b) 36-slot 8-pole machine

Figure 5.16: Cogging torque

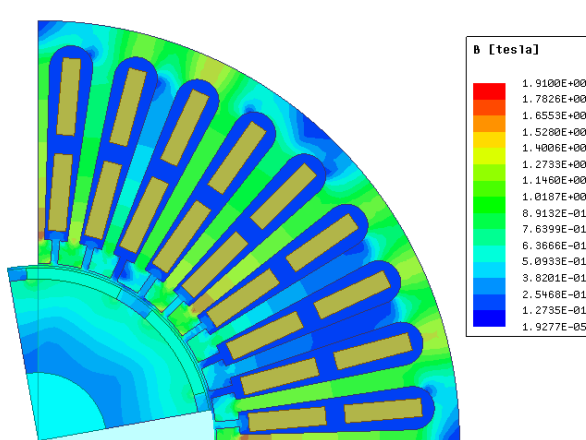


(a) 12s10p(S)

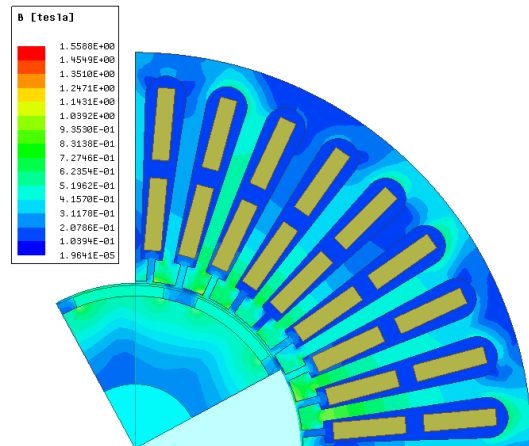


(b) 12s10p(D)

Figure 5.17: Flux densities of 12-slot machines at 1500 rpm



(a) Flux densities at 1500 rpm



(b) Flux densities at 5000 rpm

Figure 5.18: Flux densities of 36-slot machine

Chapter 6

Conclusion and Further work

6.1. Conclusion

This report detailed the concepts surrounding fractional slot SPMs in the context of EVs, described the design of three such machines and the comparison of their performance. Comparison of the machines, subject to the given constraints, show the 12-slot double-layer machine to deliver the required performance at the lowest cost with the added benefit of ease of manufacturing. The 36-slot machine provides the greatest flux weakening ability and CPSR due its high synchronous inductance, while featuring a slightly smaller cogging torque compared to the 12-slot double-layer machine due to smaller slot openings. The design process used was found to be sufficient and is reproducible should future machines need to be designed.

6.2. Recommendations for future work

While the motors have been evaluated using FEA software, which is considered to be very accurate, the motors need to be built to truly evaluate and compare the advantages of the different configurations. A very important aspect would be the evaluation of the demagnetisation aspects of the machines, which may change some design aspects as shown in [6]. Additional losses, such as friction and windage losses, can be evaluated in this way. Furthermore, the performance of the motor when used in conjunction with a flux-weakening control system must be investigated. Fault tolerance can also then be evaluated. With practicality in mind, performance of the motors can be evaluated under the constraint of a fixed outer diameter.

Possible improvements to the motors include investigating the effect of tooth shape, tooth tip shaping effects due to chamfers and reduction of cogging torque and torque ripple through the use of closed stator slots and skewing [38], [39]. The possible negative effects of these design choices, such as voltage distortion, must also be considered [40]. Furthermore, the full advantage of FSCW machines could be fully exploited by using modular stator manufacturing techniques to increase slot fill factor and thereby power density [15].

Bibliography

- [1] J. Wang, X. Yuan, and K. Atallah, "Design Optimization of a Surface-Mounted Permanent-Magnet Motor With Concentrated Windings for Electric Vehicle Applications," *IEEE Transactions on Vehicular Technology*, vol. 62, no. 3, pp. 1053–1064, 2013.
- [2] S. Hosseinpour, H. Chen, and H. Tang, "Barriers to the wide adoption of electric vehicles: A literature review based discussion," in *2015 Portland International Conference on Management of Engineering and Technology (PICMET)*, 2015, pp. 2329–2336.
- [3] B. Qu, Q. Yang, Y. Li, M. Sotelo, S. Ma, and Z. Li, "A Novel Surface Inset Permanent Magnet Synchronous Motor for Electric Vehicles," *Symmetry*, vol. 12, p. 179, 2020.
- [4] W. Lee, S. Li, D. Han, B. Sarlioglu, T. A. Minav, and M. Pietola, "A Review of Integrated Motor Drive and Wide-Bandgap Power Electronics for High-Performance Electro-Hydrostatic Actuators," *IEEE Transactions on Transportation Electrification*, vol. 4, no. 3, pp. 684–693, 2018.
- [5] J. Wang, Y. Li, and Y. Han, "Integrated Modular Motor Drive Design With GaN Power FETs," *IEEE Transactions on Industry Applications*, vol. 51, no. 4, pp. 3198–3207, 2015.
- [6] S. Pastellides, S. Gerber, R. J. Wang, and M. J. Kamper, "Design of a Surface-Mounted PM Motor for Improved Flux Weakening Performance," *ICEM*, vol. 31, no. 1, pp. 1772–1778, 2020.
- [7] M. Ehsani, Y. Gao, S. Gay, and A. Emadi, *Modern Electric, Hybrid Electric, and Fuel Cell Vehicles*. Boca Raton, Florida: CRC Press, 2004.
- [8] P. M. Tlali, R. Wang, and S. Gerber, "Magnetic gear technologies: A review," in *2014 International Conference on Electrical Machines (ICEM)*, 2014, pp. 544–550.
- [9] I. D. Kakoudakis, E. K. Karamanis, I. I. Kikidis, and A. G. Kladas, "Comparison of Permanent Magnet Motor Configurations for Electric Vehicle Applications," in *2018 XIII International Conference on Electrical Machines (ICEM)*, 2018, pp. 2058–2064.
- [10] P. Shewane, A. Singh, M. Gite, and A. Narkhede, "An Overview of Neodymium Magnets over Normal Magnets for the Generation of Energy," *International Journal*

- on *Recent and Innovation Trends in Computing and Communication*, vol. 2, no. 12, pp. 4056–4059, 2014.
- [11] D. Prosperi, A. Bevan, G. Ugalde, C. Tudor, G. Furlan, S. Dove, P. Lucia, and M. Zakotnik, “Performance comparison of motors fitted with magnet-to-magnet recycled or conventionally manufactured sintered NdFeB,” *Journal of Magnetism and Magnetic Materials*, vol. 460, pp. 448–453, 2018.
 - [12] Y. Kim, S. Lee, E. Lee, B. Cho, and S. Kwon, “Comparison of IPM and SPM motors using ferrite magnets for low-voltage traction systems,” in *2015: EVS28 International Electric Vehicle Symposium and Exhibition*, 2015, pp. 1–7.
 - [13] S. Pastellides, S. Gerber, and R. J. Wang, “Design Strategy and Comparison of Four PM Motor Topologies for a 2kW Traction Application,” in *2019 Southern African Universities Power Engineering Conference/Robotics and Mechatronics/Pattern Recognition Association of South Africa (SAUPEC/RobMech/PRASA)*, 2019, pp. 358–363.
 - [14] T. J. A.M. EL-Refaie, “Optimal flux weakening in surface pm machines using fractional-slot concentrated windings,” *IEEE Transactions on Industry Applications*, vol. 41, no. 3, pp. 790–800, May/June 2005.
 - [15] A. M. EL-Refaie, “Fractional-Slot Concentrated-Windings Synchronous Permanent Magnet Machines: Opportunities and Challenges,” *IEEE Transactions on Industrial Electronics*, vol. 57, no. 1, pp. 107–121, 2010.
 - [16] E. Carraro, N. Bianchi, S. Zhang, and M. Koch, “Design and Performance Comparison of Fractional Slot Concentrated Winding Spoke Type Synchronous Motors With Different Slot-Pole Combinations,” *IEEE Transactions on Industry Applications*, vol. 54, no. 3, pp. 2276–2284, 2018.
 - [17] S. Umans, *Fitzgerald & Kingsley’s Electric Machinery*. McGraw-Hill Education, 2013. [Online]. Available: <https://books.google.co.za/books?id=REI9XwAACAAJ>
 - [18] D. Ishak, Z. Q. Zhu, and D. Howe, “Comparison of PM brushless motors, having either all teeth or alternate teeth wound,” *IEEE Transactions on Energy Conversion*, vol. 21, no. 1, pp. 95–103, 2006.
 - [19] J. P. H. Hrabovcova, T. Jokinen, *Design of Rotating Electrical Machines*. John Wiley & Sons, Ltd, 2008.
 - [20] T. M. Jahns, “Flux-Weakening Regime Operation of an Interior Permanent-Magnet Synchronous Motor Drive,” *IEEE Transactions on Industry Applications*, vol. IA-23, no. 4, pp. 681–689, 1987.

- [21] L. Jolly, M. A. Jabbar, and Liu Qinghua, "Optimization of the constant power speed range of a saturated permanent-magnet synchronous motor," *IEEE Transactions on Industry Applications*, vol. 42, no. 4, pp. 1024–1030, 2006.
- [22] H. Liu, Z. Q. Zhu, E. Mohamed, Y. Fu, and X. Qi, "Flux-Weakening Control of Nonsalient Pole PMSM Having Large Winding Inductance, Accounting for Resistive Voltage Drop and Inverter Nonlinearities," *IEEE Transactions on Power Electronics*, vol. 27, no. 2, pp. 942–952, 2012.
- [23] W. L. Soong and T. J. E. Miller, "Field-weakening performance of brushless synchronous AC motor drives," *IEE Proceedings - Electric Power Applications*, vol. 141, no. 6, pp. 331–340, 1994.
- [24] EMETOR. (2020) Winding factor. [Online]. Available: <https://www.emetor.com/glossary/winding-factor/>
- [25] e. a. Y.Tang, "Investigation of winding topologies for permanent magnet in-wheel motors," *The International Journal for Computation and Mathematics in Electrical and Electronic Engineering*, vol. 31, no. 1, pp. 88–107, 2012.
- [26] L. Alberti and N. Bianchi, "Theory and design of fractional-slot multilayer windings," in *2011 IEEE Energy Conversion Congress and Exposition*, 2011, pp. 3112–3119.
- [27] S. Vaschetto, A. Tenconi, and G. Bramerdorfer, "Sizing procedure of surface mounted PM machines for fast analytical evaluations," in *2017 IEEE International Electric Machines and Drives Conference (IEMDC)*, 2017, pp. 1–8.
- [28] A. Sorgdrager, "Development of a line-start permanent-magnet synchronous machine," Master's thesis, North-West University, North-West University, November 2014.
- [29] Z. Q. Zhu and D. Howe, "Influence of design parameters on cogging torque in permanent magnet machines," *IEEE Transactions on Energy Conversion*, vol. 15, no. 4, pp. 407–412, 2000.
- [30] D. Wu and Z. Q. Zhu, "Design Tradeoff Between Cogging Torque and Torque Ripple in Fractional Slot Surface-Mounted Permanent Magnet Machines," *IEEE Transactions on Magnetics*, vol. 51, no. 11, pp. 1–4, 2015.
- [31] N. Bianchi and S. Bolognani, "Design optimisation of electric motors by genetic algorithms," *IEE Proceedings - Electric Power Applications*, vol. 145, no. 5, pp. 475–483, 1998.
- [32] R. Ramarathnam, B. G. Desai, and V. S. Rao, "A Comparative Study of Minimization Techniques for Optimization of Induction Motor Design," *IEEE Transactions on Power Apparatus and Systems*, vol. PAS-92, no. 5, pp. 1448–1454, 1973.

- [33] S. Rao, *Engineering Optimisation: Theory and Practice*. John Wiley & Sons, Ltd, 2009.
- [34] Y. Duan, R. G. Harley, and T. G. Habetler, “Method for multi-objective optimized designs of Surface Mount Permanent Magnet motors with concentrated or distributed stator windings,” in *2009 IEEE International Electric Machines and Drives Conference*, 2009, pp. 323–328.
- [35] M. Mutluer and O. Bilgin, “Design optimization of PMSM by particle swarm optimization and genetic algorithm,” in *2012 International Symposium on Innovations in Intelligent Systems and Applications*, 2012, pp. 1–4.
- [36] W. Gu, X. Zhu, L. Quan, and Y. Du, “Design and Optimization of Permanent Magnet Brushless Machines for Electric Vehicle Applications,” *Energies*, vol. 8, no. 12, pp. 13 996–14 008, 2015.
- [37] Y. Duan, “Method for Design and Optimization of Surface Mount Permanent Magnet Machines and Induction Machine,” Ph.D. dissertation, School of Elect. and Computer Eng., Georgia Institute of Tech., Atlanta, GA, USA, 2010.
- [38] N. Soda and M. Enokizono, “Relation Between Stator Core Shape and Torque Ripple for SPM Motor,” in *2018 XIII International Conference on Electrical Machines (ICEM)*, 2018, pp. 955–960.
- [39] K. Seo, Y. Kim, and S. Jung, “Stator teeth shape design for torque ripple reduction in surface-mounted permanent magnet synchronous motor,” in *2014 17th International Conference on Electrical Machines and Systems (ICEMS)*, 2014, pp. 387–390.
- [40] D. Wu, Z. Q. Zhu, and X. Ge, “Effectiveness of Terminal Voltage Distortion Minimization Methods in Fractional Slot Surface-Mounted Permanent Magnet Machines Considering Local Magnetic Saturation,” *IEEE Transactions on Energy Conversion*, vol. 31, no. 3, pp. 1090–1099, 2016.

Appendix A

Project Planning Schedule

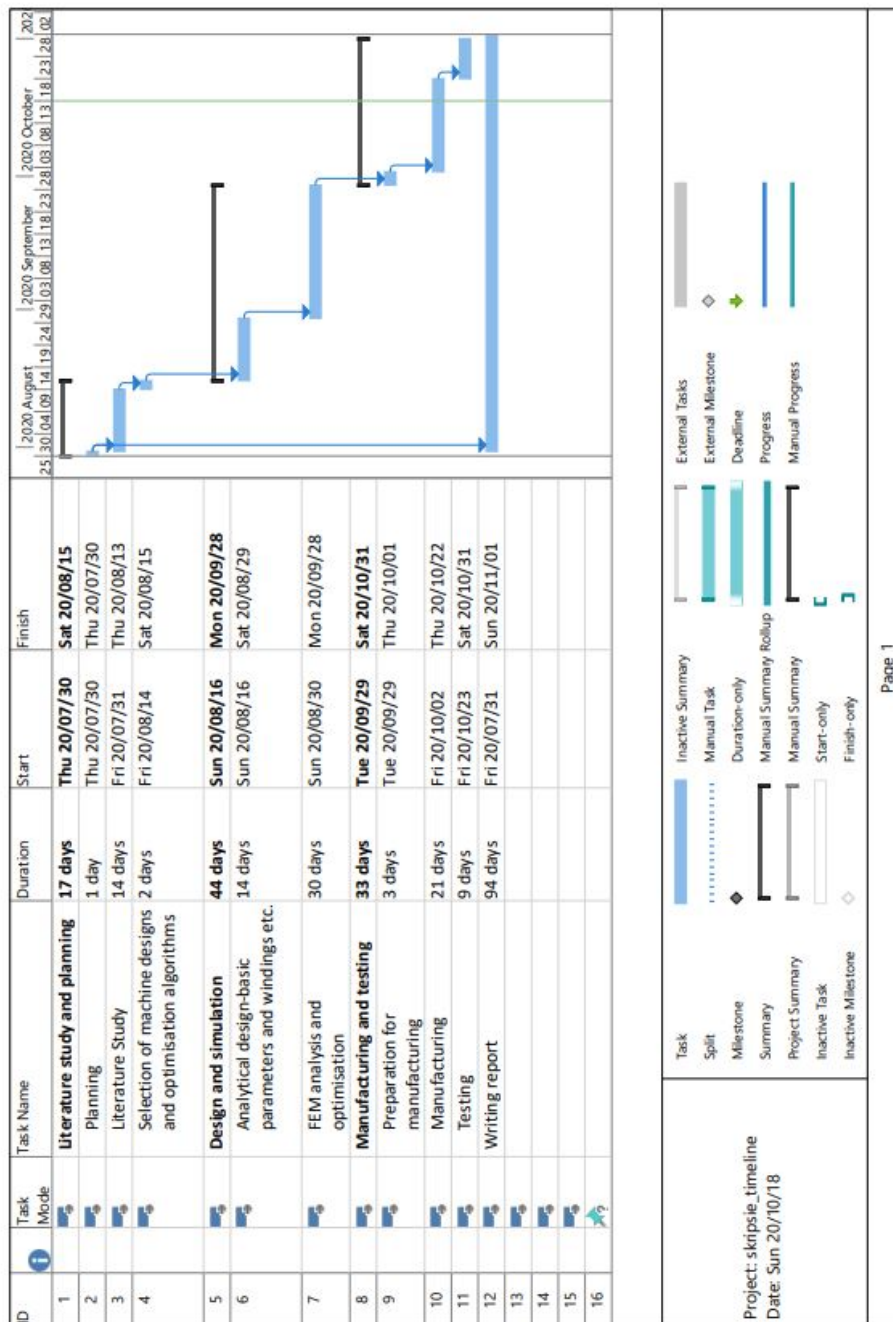


Figure A.1: Initial planning

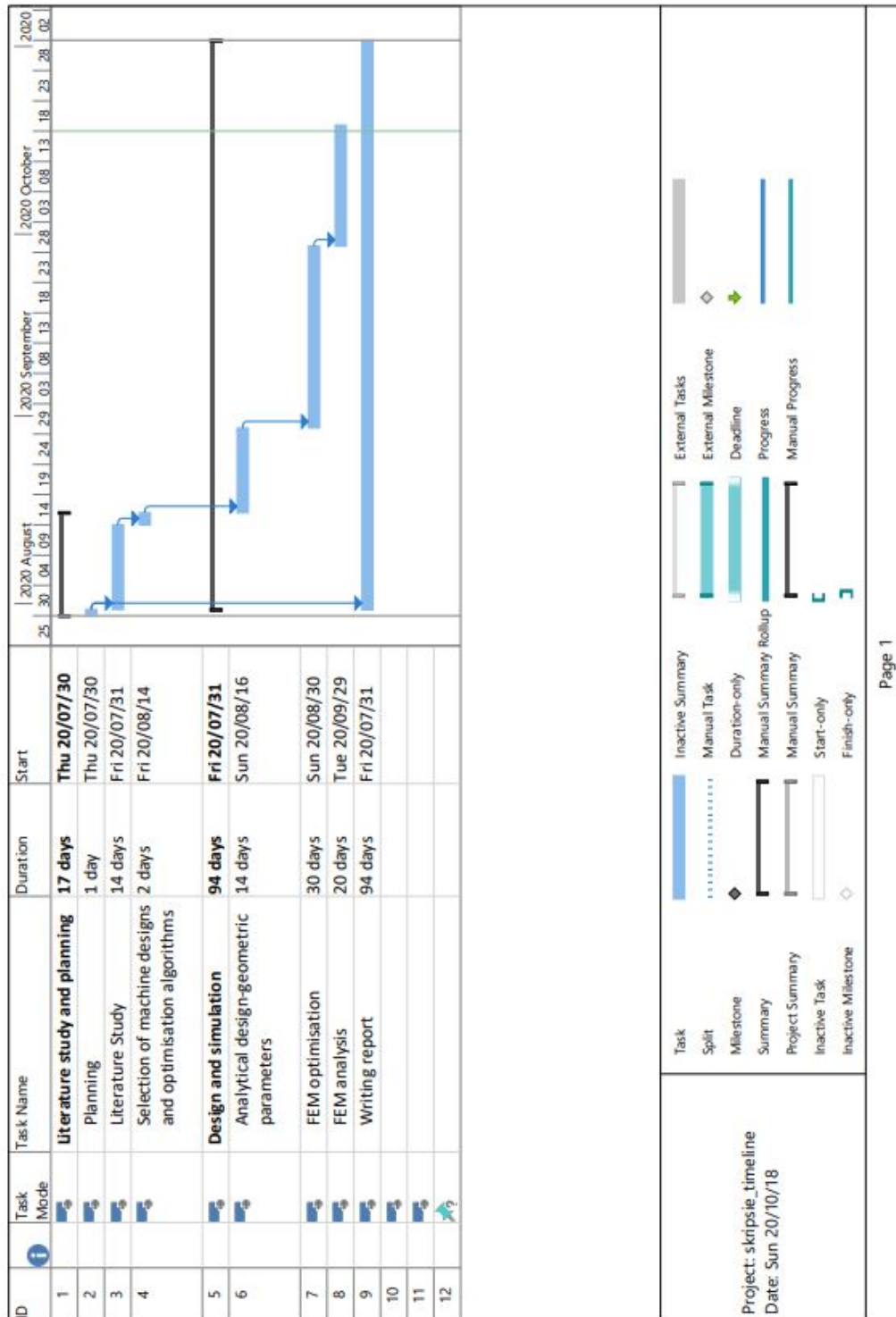


Figure A.2: Revised planning

Appendix B

Outcomes Compliance

B.1. ELO 1: Problem solving

The initial problem is stated to be the comparison and analysis of different SPM synchronous motors with unconventional winding topologies, in the context of use in electric vehicles. Firstly, this problem statement requires understanding these technologies, as discussed in Chapter 2 of this report where electric vehicles, PM technology and winding topologies are discussed. Chapter 3 provides some of the characteristics in terms of the machine attributes and the operation of these machines under flux-weakening control - a very popular control method.

A secondary problem is the design process of these machines. This requires a design process to be developed, starting from initial machine specifications (externally determined in this case) and narrowing it down to obtain the exact physical dimensions of the machine. As described in Chapter 4, the process consists of 2 parts. Firstly, an analytical method is used to determine initial geometric parameters of the machine. While providing a starting point, this method alone cannot ensure all specifications are met in the most effective way. Thus, the second part of the process involves a design optimisation through the use of software to ensure specifications are adhered to in the entire operational range of the machine and that it is done in the most cost-effective way, a very practical consideration.

With the design stage completed, the machines must be analysed and conclusions drawn from results obtained. This is done in Chapter 5, where the results of the different machine designs are shown and discussed. Possible reasons for differences and performance are discussed, based on theory from literature also discussed in earlier chapters and from additional analysis relying on knowledge from undergraduate modules.

B.2. ELO 2: Application of scientific and engineering knowledge

This outcome is achieved through the use of scientific and engineering knowledge throughout the project. Firstly, the basic working principles of synchronous motors must be understood, relying on modelling of these machines, based on electromagnetic theory, through circuit

diagrams, phasor diagrams and equations as shown in Chapter 3. To design physical dimensions of the machines, these electromagnetic principles must now be combined with practical sizing considerations to obtain dimensions as shown in Chapter 4. To analyse the machines, the underlying principles must be understood so that conclusions can be drawn from results, as shown in Chapter 5.

B.3. ELO 3: Engineering design

This outcome is achieved through the implementation of procedural and non-procedural design methods. The main design aspect of the project is the design of three different machines, starting with an initial set of specifications and ending with three machines which conform to these specifications, based on simulation and analysis. The machine design process is formalised as much as possible, to ensure it is reproducible with as much detail as possible provided in Chapter 4. However, it consists of less formally structured parts, such as the machine optimisation, also described in Chapter 4, and practical considerations implemented in Chapter 5.

B.4. ELO 4: Investigations, experiments and data analysis

Various motor topologies featuring overlapping and non-overlapping windings were investigated based on tractive effort required and other specifications. The performance characteristics of each identified candidate design were calculated using coupled-field circuits as explained in Chapter 4. The machines were then analysed under various conditions to ensure specifications were met using two different FEA software packages, SEMFEM and ANSYS MAXwell. The results obtained were then processed to be analysed and discussed, as shown in Chapter 5, with possible reasons provided for performance. Further analysis over the entire speed range of the motors is shown in Appendix C.

B.5. ELO 5: Engineering methods, skills and tools, including Information Technology

This outcome is demonstrated through the use of various software tools. MATLAB was used to plot data and to effectively perform calculations, especially iterative calculations such as the calculation of geometric parameters described in Section 4.4. Analysis, simulation and optimisation of the machines was performed in two software packages, ANSYS Maxwell and SEMFEM. The SEMFEM package required the use of the Python programming

language. Report writing was performed using a L^AT_EX compiler while diagrams were drawn using both Microsoft Excel and draw.io, an online diagram editor.

B.6. ELO 6: Professional and technical communication

This outcome is demonstrated through this report, the oral presentation and accompanying slides as well as the project poster. It is further achieved through the effective communication of technical information through the use of equations and diagrams. Results are presented effectively through figures and tables. Weekly meetings with my supervisor served as verbal professional communication, with additional correspondence via email.

B.7. ELO 8: Individual work

This outcome is firstly demonstrated by completion of this project and the report which required large amounts of individual work. Furthermore, the design method, choice of machines to investigate and conclusions drawn from analysis are my own based on literature and guidance from my study leader. Various aspects had to be collected from different sources and combined to create this report as shown in Chapter 2, 3 and 4, demonstrating this outcome.

B.8. ELO 9: Independent Learning Ability

This outcome is demonstrated by obtaining the necessary knowledge to design, optimise and analyse SPM synchronous motors. This required knowledge of the following aspects which were not obtained through undergraduate modules: SPM synchronous motors, winding topologies and the layout thereof, flux-weakening operation, design of the physical dimensions of machines, machine optimisation, use of FEA software and use of the programming language Python. Knowledge was obtained through conference papers, journal articles, textbooks and software training events.

Appendix C

Additional results, equations and derivations

C.1. Flux density, thermal(current) aspects and efficiency maps

The flux densities in the 12-slot machines at 5000 rpm are shown in Fig. C.1, illustrating the weakening of the flux in the machines when compared to the flux densities shown in Fig. 5.17 at 1500 rpm. The linear current densities, K_s and current densities, J , of the final machines are shown in Table C.1.

The efficiency and loss maps of the 12-slot single-layer machine are shown in Fig. C.2 and C.3 respectively. The efficiency and loss maps of the 12-slot double-layer machine are shown in Fig. C.4 and C.5 respectively. The efficiency and loss maps of the 36-slot machine are shown in Fig. C.6 and C.7 respectively. All three machines show wide ranges of high efficiency. The 12-slot single-layer machines shows the lowest losses at low speeds relative to its losses at high speed, while the 36-slot machine shows high losses over the entire speed range when operated at the maximum torque value at all respective speeds.

C.2. Results from SEMFEM simulations

Additional results obtained from preliminary simulations is shown in Tables C.2 and C.3 below.

Table C.1: Current limits for air-cooled PMSMs

Final value	12s10p(S)	12s10p(D)	36s8p(D)
K_s (kA/m)	51.36	47.387	60.31
J (A/mm ²)	5.12	5.002	4.981

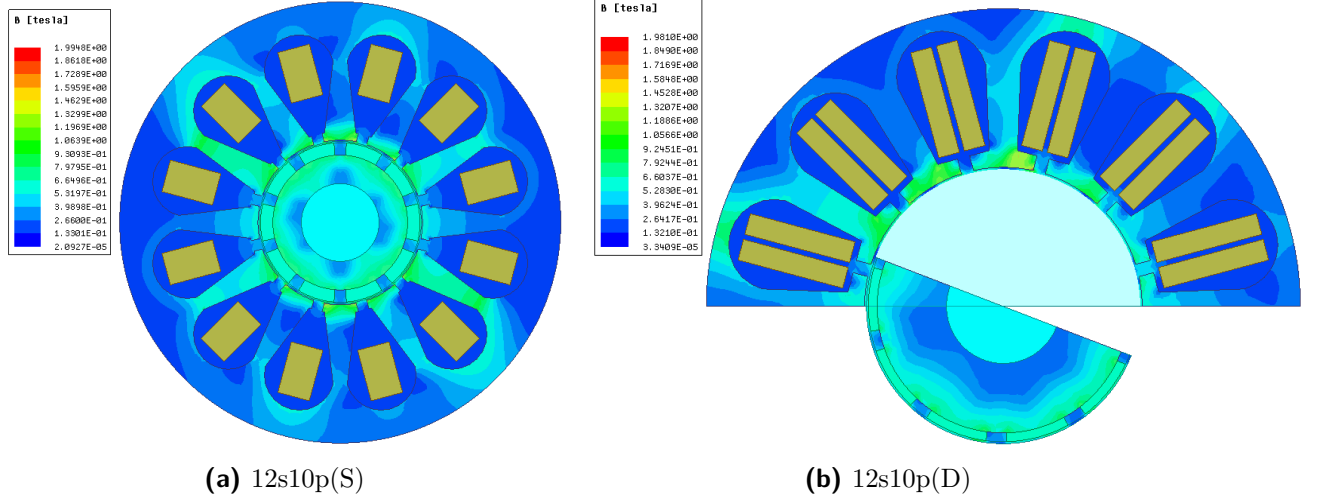


Figure C.1: Flux densities of 12-slot machines at 5000 rpm

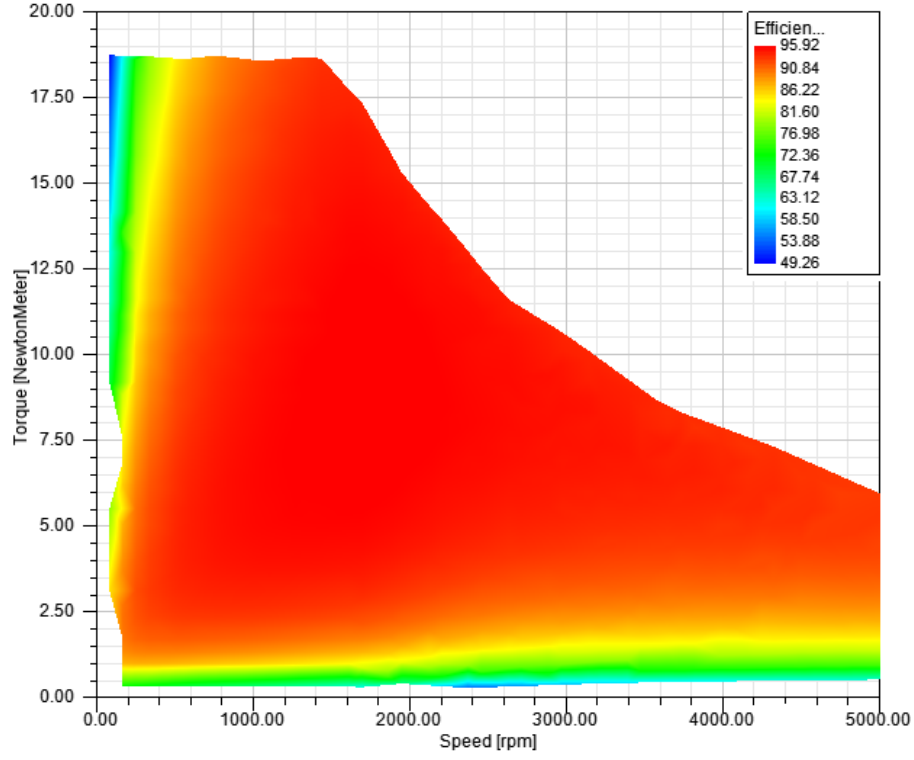


Figure C.2: Efficiency map of 12-slot single-layer machine

Table C.2: Preliminary design results at 1500 rpm (SEMFEM)

Parameter	12s10p(S)	12s10p(D)	36s8p(D)
Current density [J]	4.152 A/mm ²	4.55 A/mm ²	4.038 A/mm ²
d-axis current [i_d]	-38.433 A	-36.78 A	-36.403 A
q-axis current [i_q]	47.138 A	47.818 A	48.297 A
d-axis flux linkage [λ_d]	21.938 mWb	23.791 mWb	31.854 mWb
q-axis flux linkage [λ_q]	41.812 mWb	41.23 mWb	50.196 mWb

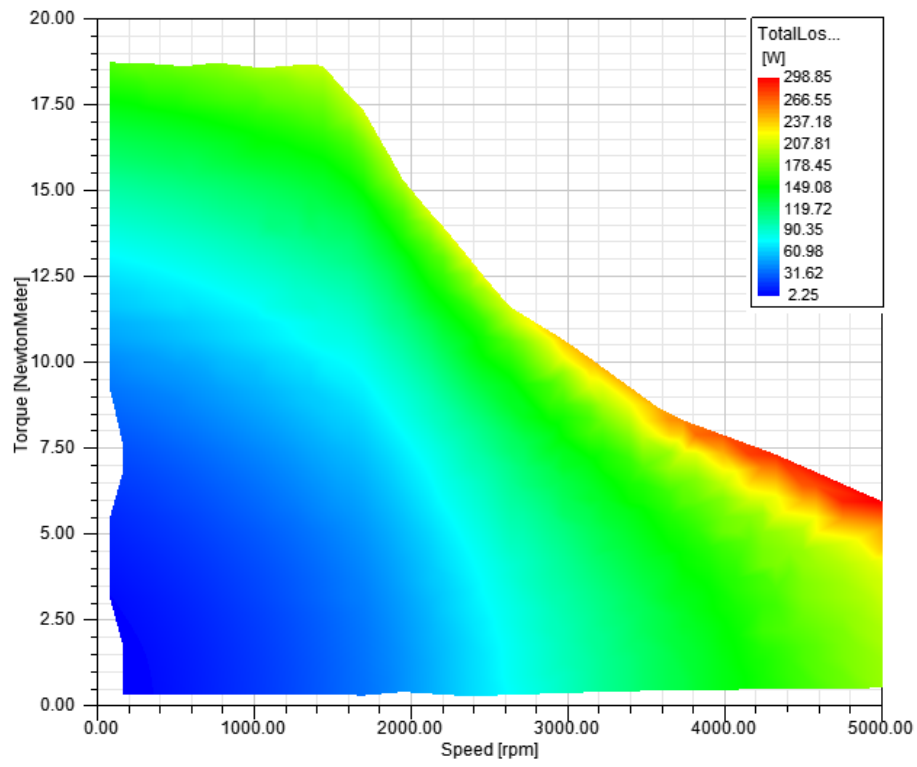


Figure C.3: Loss map of 12-slot single-layer machine

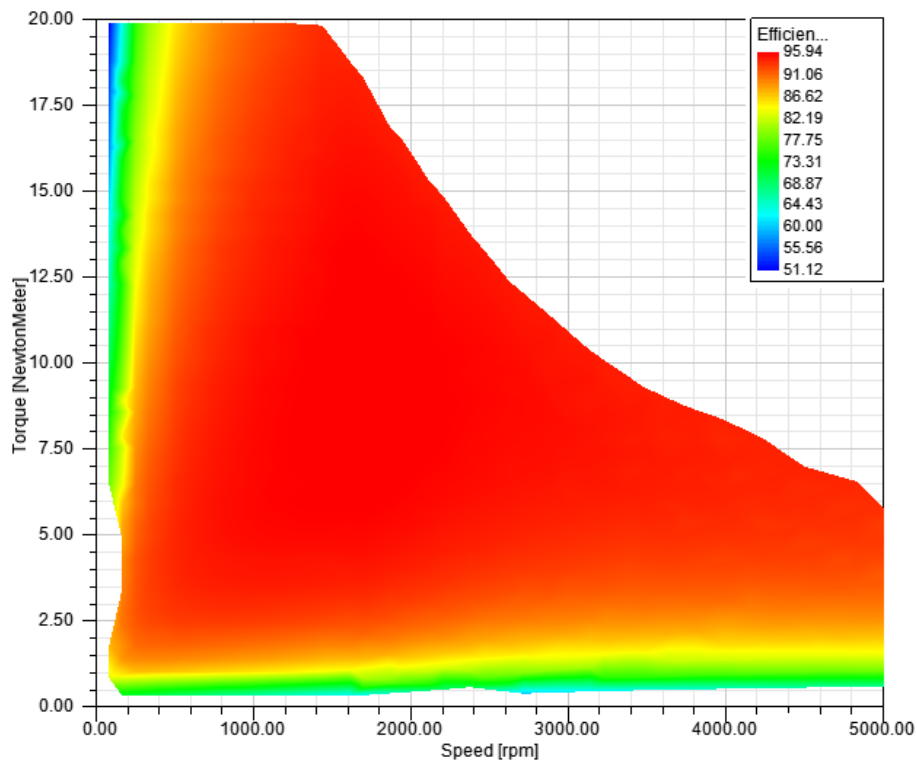


Figure C.4: Efficiency map of 12-slot double-layer machine

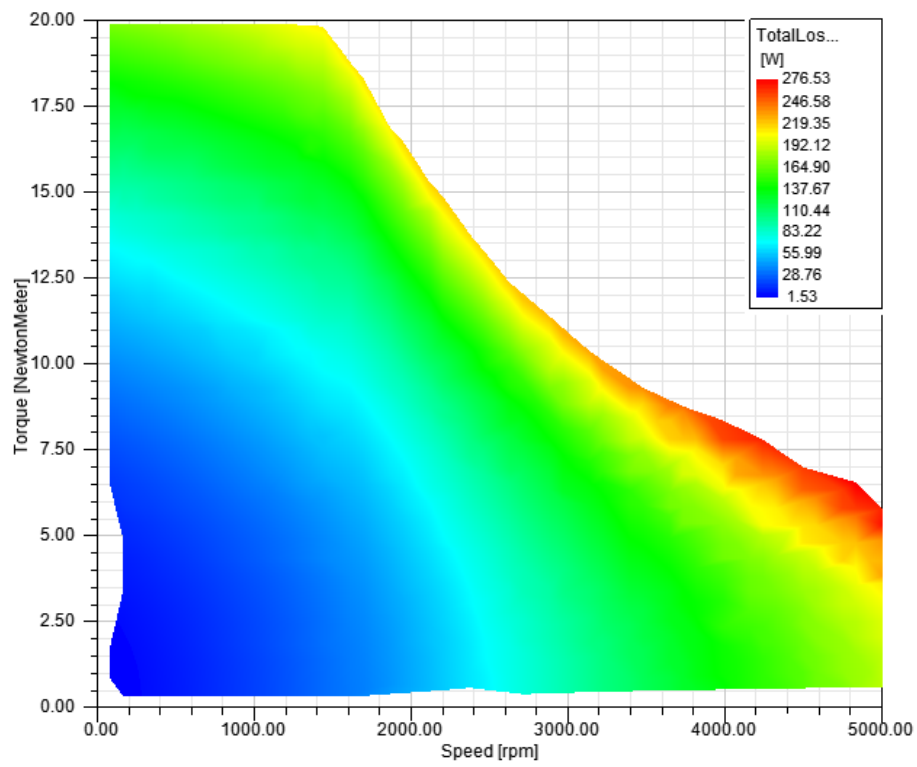


Figure C.5: Loss map of 12-slot double-layer machine

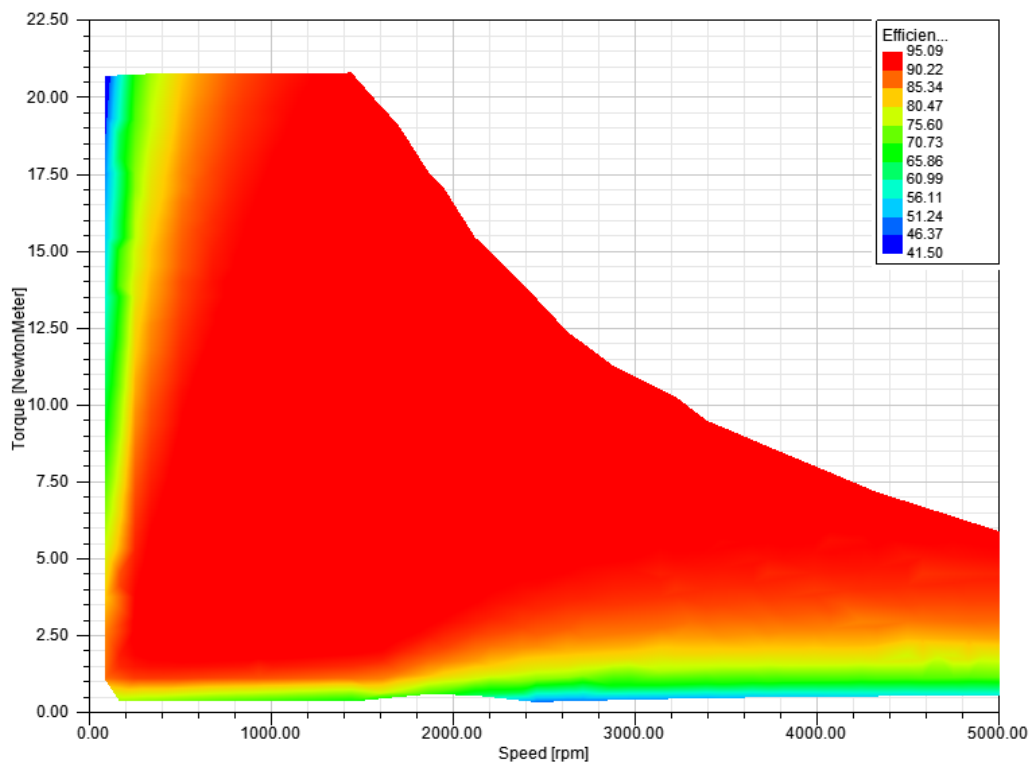


Figure C.6: Efficiency map of 36-slot machine

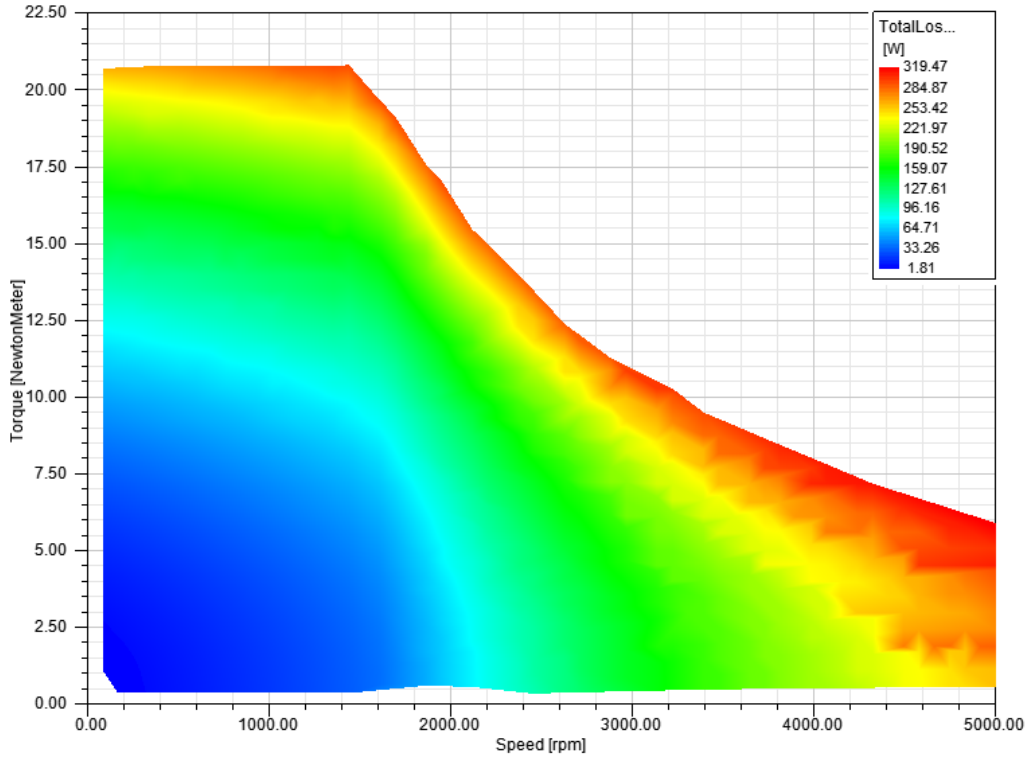


Figure C.7: Loss map of 36-slot machine

Table C.3: Preliminary design results at 5000 rpm (SEMFEM)

Parameter	12s10p(S)	12s10p(D)	36s8p(D)
Current density [J]	3.949 A/mm ²	4.445 A/mm ²	3.993 A/mm ²
d-axis current [i_d]	-58.77 A	-58.453 A	-58.447 A
q-axis current [i_q]	15.94 A	15.397 A	15.534 A
d-axis flux linkage [λ_d]	5.934 mWb	5.684 mWb	8.839 mWb
q-axis flux linkage [λ_q]	12.58 mWb	12.42 mWb	15.13 mWb

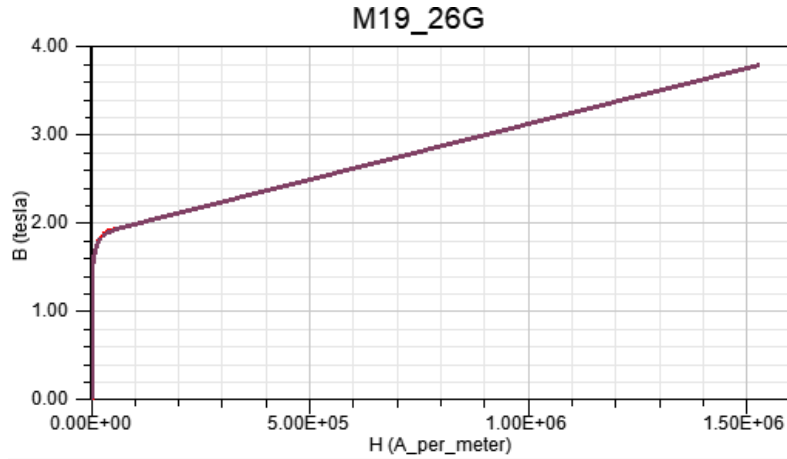


Figure C.8: M19_26G BH-curve

C.3. Electrical steel properties

The BH-curve of the M19_26G electrical steel as used in ANSYS Maxwell is shown in Fig. C.8.

C.4. Open circuit magnetic field calculation

The coefficients used for the calculation of the open-circuit magnetic field are given below, with dimensions defined as shown in Fig. C.9. Note $R_m = R_r + h_m$ and r is the radius at which the air-gap flux density is calculated.

$$A_{1n} = \frac{\sin((np+1)\alpha_p \frac{\pi}{2p})}{(np+1)\alpha_p \frac{\pi}{2p}} \quad (C.1)$$

$$A_{2n} = \frac{\sin((np-1)\alpha_p \frac{\pi}{2p})}{(np-1)\alpha_p \frac{\pi}{2p}} \quad (C.2)$$

$$M_{rn} = \frac{B_r}{\mu_0} \alpha_p (A_{1n} + A_{2n}) \quad (C.3)$$

$$M_{\theta n} = \frac{B_r}{\mu_0} \alpha_p (A_{1n} - A_{2n}) \quad (C.4)$$

$$M_n = M_{rn} + np M_{\theta n} \quad (C.5)$$

$$A_{3n} = (np - \frac{1}{np}) \frac{M_{rn}}{M_n} + \frac{1}{np} \quad (C.6)$$

$$K_{B1n} = (A_{3n} - 1) + 2(\frac{R_r}{R_m})^{np+1} - (A_{3n} + 1)(\frac{R_r}{R_m})^{2np} \quad (C.7)$$

$$K_{B2n} = \frac{\mu_r + 1}{\mu_r} (1 - (\frac{R_r}{R_{is}})^{2np}) - \frac{\mu_r - 1}{\mu_r} ((\frac{R_m}{R_{is}})^{2np} - (\frac{R_r}{R_m})^{2np}) \quad (C.8)$$

$$K_{B3n} = \frac{np}{(np)^2 - 1} \quad (C.9)$$

$$K_{Bn} = \frac{\mu_0 M_n}{\mu_r} K_{B3n} \frac{K_{B1n}}{K_{B2n}} \quad (C.10)$$

$$f_{Brn} = (\frac{r}{R_{is}})^{np-1} (\frac{R_m}{R_{is}})^{np+1} (\frac{R_m}{r})^{np+1} \quad (C.11)$$

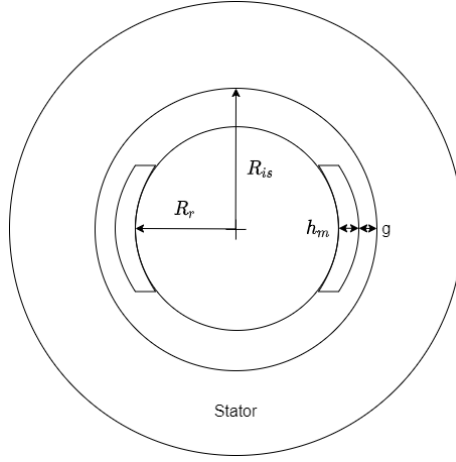


Figure C.9: Machine dimensions

C.5. Additional inductance and resistance calculations

For Eq. 3.6, τ_p is defined as shown in Eq. 4.16, g_{eff} as shown in Eq. C.12 and l' as shown in Eq. C.13.

$$g_{eff} = \frac{h_m}{\mu_r} + g \quad (\text{C.12})$$

$$l' = l + 2g \quad (\text{C.13})$$

Additional slot leakage parameters are given below in Eq. C.14 to Eq. C.16.

$$k_1 = 1 - \frac{9}{16}\epsilon \quad (\text{C.14})$$

$$k_2 = 1 - \frac{3}{4}\epsilon \quad (\text{C.15})$$

$$\epsilon = 1 - \frac{W}{\tau_p} \quad (\text{C.16})$$

The coil length, as used in Eq. 3.10, is given in Eq. C.17. Note $W = \frac{\gamma}{\gamma_Q} \tau_p$.

$$l_c = 2l + 2.4W + 0.1 \quad (\text{C.17})$$

Appendix D

MATLAB design scripts

The design script as used in MATLAB to obtain initial geometric parameters is shown below. Note only the script for the 12-slot 10-pole single-layer winding machine is shown as the same script was used for the other machines, with appropriate inputs parameters changed. Also note that to use this script for distributed winding machines, Eq. 4.20 and Eq. 4.18 must be used.

```
1 clear all;
2 %Rated data
3 Tr = 19.1;
4 nr = 1500;
5 Vr = 48;
6
7 %Material
8 Br = 1.2899;
9 ur = 1.05;
10 Ki = 0.95;
11 u0 = 4*pi*10^(-7);
12 %Material stress loadings
13 %maximum stator yoke flux
14 Bysmax = 1;
15 %maximum stator teeth flux
16 Btsmax = 1.6;
17 %maximum rotor yoke flux
18 Byrmax = 1;
19 %current density in A/mm^2
20 J = 4;
21
22 %Geometrical and winding specs
23 lambda = 1;
24 %number of poles, q, chosen short pitch ratio and number of coils per
    phase
25 poles = 10;
26 q = 0.4;
27 Qs = 12;
28 yQ = 5/6;
29 numCoils = 2;
30 %shaft diameter in mm
```

```

31 Dmin = 30;
32 Dir = Dmin;
33 %air gap thickness in mm
34 hag = 1;
35 %magnet thickness in mm
36 lm = 3;
37 %magnet to pole coverage ratio
38 alpham = 0.83;
39 %slot opening in mm
40 w0 = 2;
41 %slot enclosure dimensions in mm
42 h11 = 2;
43 h12 = 2;
44 %fill factor as percentage
45 kfill = 35;
46 %fundamental winding factor
47 Kw1 = 0.966;
48
49 %Calculate Bg
50 lmacc = lm/ur;
51 %assume Kc= 1.05
52 hagacc = hag*1.05;
53 Bg = Br * (lmacc/(lmacc + hagacc));
54 Bg1 = (4/pi)*Bg*sin(alpham*(pi/2));
55
56 %Calculate new parameters
57 C1 = ((sqrt(2)*pi)/4);
58 %linear current density
59 KsAperm = 350*100;
60 %air gap diameter in mm
61 Dag2 = (nthroot((Tr/(C1*Bg1*KsAperm*lambda)),3))*1000;
62 %axial length in mm
63 Lcore2 = lambda*Dag2;
64 %External rotor diameter - measured at outside of rotor yoke in mm
65 Der2 = Dag2 - 2*lm - 2*(hag/2);
66 %internal stator diameter in mm
67 Dis2 = Dag2 + 2*(hag/2)
68 taup = (pi*Dis2)/poles;
69 taus = (pi*Dis2)/(Qs);
70 %in mm
71 hys2 = (Bg/(Bysmax*Ki))*(alpham*taup-((taus - taup)/2));
72 wtt2 = (Bg/(Btsmax*Ki))*(alpham*taup-((taus - taup)/2));
73 h1 = h11+h12;
74 Dh12 = Dis2 + 2*h1;
75 wst2 = ((pi*Dh12)/Qs)-wtt2;
76 %usable slot area in m^2
77 Aus2 = (KsAperm*pi*(Dh12/1000))/((J*10^6)*Qs*Kw1*(kfill/100));

```

```

78 %in mm^2
79 Aus2 = Aus2*10^6;
80 hus2 = ((-1*wst2) + sqrt(wst2^2+(4*pi*Aus2/Qs)))/(2*pi/Qs);
81 %external stator diameter in mm
82 Des2 = Dh12+2*(hus2+hys2);
83 wsb2 = (pi*(Dh12+2*hus2)/Qs)-wtt2;
84 hts2 = hus2+h1;
85 refspeed = 1500;
86 fr = refspeed*poles/120;
87 omegar = 2*pi*fr;
88 lacc = Lcore2 + 2*hag;
89 taup = (pi*Dis2)/poles;
90 %number of truns per phase
91 Nph = (sqrt(2)*(Vr/sqrt(3)))/(omegar*Kw1*alphan*Bg1*(taup/1000)*(lacc
    /1000));
92 %choose number of turns per phase - integer value
93 Nphchoice = 30;
94 %number of conductors per slot
95 zQ = (6/Qs)*Nphchoice;
96 %recalculate new Bg1 to check it does not vary too much
97 Bg1new = (sqrt(2)*(Vr/sqrt(3)))/(omegar*Kw1*alphan*Nphchoice*(taup/1000)
    *(lacc/1000));
98 %magnet width
99 wm = alphan*taup;
100 %use m units
101 fluxp = Bg*(wm/1000).*(Lcore2/1000);
102 fluxp1 = (2/pi)*Bg1new*(taup/1000)*(Lcore2/1000);
103 %flux in rotor yoke
104 Byr = (fluxp/2)/((((Der2-Dir)/2)/1000)*(Lcore2/1000)*Ki);
105 %calculate number of turns per coil
106 Ncoil = Nphchoice/numCoils;
107 %write data to text file
108 fileID = fopen('initialParams.txt','w');
109 fprintf(fileID,'% -25s % -22s\n', 'Dimensions', 'Value(all units in mm)');
110 fprintf(fileID,'% -25s %22.2f\n', 'Air gap(g)',hag);
111 fprintf(fileID,'% -25s %22.2f\n', 'Magnet thickness(hpm)',lm);
112 fprintf(fileID,'% -25s %22.2f\n', 'Magnet coverage',alphan);
113 fprintf(fileID,'% -25s %22.2f\n', 'Dag2',Dag2);
114 fprintf(fileID,'% -25s %22.2f\n', 'Lcore2',Lcore2);
115 fprintf(fileID,'% -25s %22.2f\n', 'Inner stat diam(Dis)',Dis2);
116 fprintf(fileID,'% -25s %22.2f\n', 'Rotor ext diam(Der)',Der2);
117 fprintf(fileID,'% -25s %22.2f\n', 'Stator yoke height(hys)',hys2);
118 fprintf(fileID,'% -12s %22.2f\n\n', 'External stator diam(Des)',Des2);
119 fprintf(fileID,'% -25s % -22s\n', 'Slot Dimensions', 'Value(all units in
    mm)');
120 fprintf(fileID,'% -25s %22.2f\n', 'Tooth width(wtt)',wtt2);
121 fprintf(fileID,'% -25s %22.2f\n', 'Slot opening(w0)',w0);

```

```

122 fprintf(fileID, '%-25s %22.2f\n', 'h11', h11);
123 fprintf(fileID, '%-25s %22.2f\n', 'h12', h12);
124 fprintf(fileID, '%-25s %22.2f\n', 'wst2', wst2);
125 fprintf(fileID, '%-25s %22.2f\n', 'wsb2', wsb2);
126 fprintf(fileID, '%-25s %22.2f\n', 'Usable slot height(hus)', hus2);
127 fprintf(fileID, '%-25s %22.2f\n', 'Usable slot area(Aus)', Aus2);
128 fprintf(fileID, '%-25s %22.2f\n\n', 'Fill factor(kfill)', kfill);
129 fprintf(fileID, '%-25s %-22s\n', 'Electrical aspects', 'Values');
130 fprintf(fileID, '%-25s %22.2f\n', 'Nph', Nph);
131 fprintf(fileID, '%-25s %22.2f\n', 'Nphchoice', Nphchoice);
132 fprintf(fileID, '%-25s %22.2f\n', 'Conductors per slot(zQ)', zQ);
133 fprintf(fileID, '%-25s %22.2f\n', 'Turns per coil(Ncoil)', Ncoil);
134 fprintf(fileID, '%-25s %22.2f\n', 'Linear curr dens(A/cm)', KsAperm/100);
135 fprintf(fileID, '%-25s %22.2f\n', 'J(A/mm^2)', J);
136 fprintf(fileID, '%-25s %22.2f\n\n', 'Rated voltage LL(Vr)', Vr);
137 fprintf(fileID, '%-25s %-22s\n', 'Magnetic aspects', 'Values');
138 fprintf(fileID, '%-25s %22.2f\n', 'Bg1new', Bg1new);
139 fprintf(fileID, '%-25s %22.2f\n', 'Bg1old', Bg1);
140 fprintf(fileID, '%-25s %22.2f\n', 'Byr', Byr);
141 fprintf(fileID, '%-25s %22.2f\n', 'Bys', Bysmax);
142 fprintf(fileID, '%-25s %22.2f\n', 'Bts', Btsmax);
143 fclose(fileID);

```

Listing D.1: MATLAB script

Appendix E

SEMFEM simulation code

```
1  #!/usr/bin/env python3
2  import semfem4 as sf4
3  import matplotlib.pyplot as plt
4  from math import pi
5  from math import sqrt
6  import pprint
7  import numpy as np
8  import os
9  import json
10 import sys
11 from scipy.interpolate import *
12
13 class design_simulation(sf4.simulation):
14     def draw_rotor_pole(self, v, i):
15         rotor_mesh = [v['mesh1'], v['mesh2'], v['mesh3']]
16         if i % 2 == 0:
17             ds = sf4.slots.inner_surface_pm_pole2(sf4,v['p'],v['mpp'],v[
18 'mt'],v['rot_yt'],v['r_iy'],v['r_iy'],v['Br'],v['ur'],rotor_mesh)
19         else:
20             ds = sf4.slots.inner_surface_pm_pole2(sf4,v['p'],v['mpp'],v[
21 'mt'],v['rot_yt'],v['r_iy'],v['r_iy'],-v['Br'],v['ur'],rotor_mesh)
22         return ds
23     def draw_stator_slot(self, v, i):
24         stator_dvars = [v['Q'],v['ro'],v['ro'],v['st_yt'],v['st_tt'],v[
25 'sat'],v['sot'],v['spp'],v['sop'],250]
26         stator_mesh = [v['mesh1'], v['mesh2'], v['mesh3']]
27         ds, ew = sf4.slots.outer_parallel_teeth_round_slot(sf4,self.
28 winding[i],stator_dvars,stator_mesh)
29         return ds
30     def simulate(self, m, v):
31         with open('v.json', 'w') as file:
32             file.write(json.dumps(v, indent=4))
33         # Initialize empty results dictionary
34         y = {}
35
36         # Point 1 simulation
```

```

33     self.standard_current_density_sim(m, v['steps'], v['nrpm1'], v['
idens_d1'], v['idens_q1'],
34
35     coil_ff=v['coil_ff'],
36
37     coil_turns=v['coil_turns'],
38
39     fpl_output=1)
40
41     y1 = self.standard_post(m, winding_temp=v['winding_temp'],
print_results=False)
42
43     # Point 1 results
44     y['T1'] = y1['T_av']
45     #y['T_rip1'] = ((max(self.ts.torq_vec[:, 0])) - min(self.ts.
torq_vec[:, 0]))/y1['T_av']
46     y['eff1'] = y1['eff']
47     y['Is1'] = (max(self.ts.i_vec[:,0]))/(sqrt(2))
48     y['i_d1'] = y1['i_d']
49     y['i_q1'] = y1['i_q']
50     y['i1_rms1'] = y1['i1_rms']
51     y['i_rms1'] = y1['i_rms']
52     y['idens_rms1'] = y1['idens_rms']
53     y['e_rms1'] = y1['e_rms']
54     y['u_rms1'] = y1['u_rms']
55     y['u_ll1'] = y1['u_ll']
56     y['P_out1'] = y1['P_out']
57     y['P_in1'] = y1['P_in']
58     y['P_copper1'] = y1['P_c']
59     y['P_core1'] = y1['P_core']
60     y['P_loss1'] = y1['P_loss']
61     y['PF1'] = y1['PF']
62     y['demag_margin1'] = y1['demag_margin']
63     y['fl_d11'] = y1['fl_d1']
64     y['fl_q11'] = y1['fl_q1']
65     y['fl_rms1'] = y1['fl_rms']
66     y['tcog1_max'] = max(self.ts.torq_vec[:,0])
67     y['tcog1_min'] = min(self.ts.torq_vec[:,0])
68
69     np.savetxt('torque1500.txt',self.ts.torq_vec[:,0])
70     np.savetxt('curr1500.txt',self.ts.i_vec[:,0])
71     np.savetxt('flink1500.txt',self.ts.flink_vec[:,0])
72     f_flink = splrep(self.ts.time_vec, self.ts.flink_vec[:,0], k=3)
73     voltage= splev(self.ts.time_vec, f_flink, der=1)
74     np.savetxt('voltage1500.txt',voltage)
75
76     # Point 2 simulation
77     self.standard_current_density_sim(m, v['steps'], v['nrpm2'], v['
idens_d2'], v['idens_q2'],
78
79     coil_ff=v['coil_ff'],

```

```

coil_turns=v['coil_turns'],
75
76
77         y2 = self.standard_post(m, winding_temp=v['winding_temp'],
print_results=False)
78
79         # Point 2 results
80         y['T2'] = y2['T_av']
81         #y['T_rip2'] = ((max(self.ts.torq_vec[:, 0])) - min(self.ts.
torq_vec[:, 0]))/y2['T_av']
82         y['eff2'] = y2['eff']
83         y['Is2'] = (max(self.ts.i_vec[:,0]))/(sqrt(2))
84         y['i_d2'] = y2['i_d']
85         y['i_q2'] = y2['i_q']
86         y['i1_rms2'] = y2['i1_rms']
87         y['i_rms2'] = y2['i_rms']
88         y['idens_rms2'] = y2['idens_rms']
89         y['e_rms2'] = y2['e_rms']
90         y['u_rms2'] = y2['u_rms']
91         y['u_ll2'] = y2['u_ll']
92         y['P_out2'] = y2['P_out']
93         y['P_in2'] = y2['P_in']
94         y['P_copper2'] = y2['P_c']
95         y['P_core2'] = y2['P_core']
96         y['P_loss2'] = y2['P_loss']
97         y['PF2'] = y2['PF']
98         y['demag_margin2'] = y2['demag_margin']
99         y['fl_d12'] = y2['fl_d1']
100        y['fl_q12'] = y2['fl_q1']
101        y['fl_rms2'] = y2['fl_rms']
102        y['tcog2_max'] = max(self.ts.torq_vec[:,0])
103        y['tcog2_min'] = min(self.ts.torq_vec[:,0])
104
105        np.savetxt('torque5000.txt',self.ts.torq_vec[:,0])
106        np.savetxt('curr5000.txt',self.ts.i_vec[:,0])
107        np.savetxt('flink5000.txt',self.ts.flink_vec[:,0])
108        f_flink = splrep(self.ts.time_vec, self.ts.flink_vec[:,0], k=3)
109        voltage= splev(self.ts.time_vec, f_flink, der=1)
110        np.savetxt('voltage5000.txt',voltage)
111
112        y['C_total'] = y1['C_total']
113        y['C_steel'] = y1['C_steel']
114        y['C_copper'] = y1['C_copper']
115        y['C_magnet'] = y1['C_magnet']
116        y['M_total'] = y1['M_total']
117        y['M_steel'] = y1['M_steel']
118        y['M_copper'] = y1['M_copper']

```



```

119     y['M_magnet'] = y1['M_magnet']
120     y['d_wire'] = y1['d_wire']
121     with open('output.json', 'w') as file:
122         file.write(json.dumps(y, indent=4))
123
124     return y
125
126 def setup_simulation(v):
127     v['spp'] = v['wst']/(v['wst'] + v['wtt'])
128     v['q'] = v['Q']/(2*v['p']*3)
129     v['R'] = v['Dout']/2
130     v['ro'] = v['R']
131     v['st_yt'] = v['thickSyoke']
132     v['rot_yt'] = v['thickRyoke']
133     v['sot'] = v['h1']
134     v['Dis'] = v['Dir'] + 2*v['thickRyoke'] + 2*v['mag_thick'] + 2*v['ag
135     v['st_tt'] = v['R'] - v['thickSyoke'] - v['h1'] - v['Dis']/2
136     distperSlotgap = (pi*v['Dis'])/(v['Q'])
137     v['sop'] = v['w0']/(distperSlotgap)
138     v['mpp'] = v['alphamag']
139     v['mt'] = v['mag_thick']
140     v['r_iy'] = v['Dir']/2
141     v['mesh1'] = v['mesh_scale']*1e-3
142     v['mesh2'] = v['mesh_scale']*2e-3
143     v['mesh3'] = v['mesh_scale']*3e-3
144     sim = design_simulation(2*v['p'], 2*v['p'], v['Q'], v['L'], v['Dout'
145     project=v['project'], verbosity=v['verbosity
146     return sim
147
148 if __name__ == '__main__':
149     with open('params.json', 'r') as jsonfile:
150         v = json.load(jsonfile)
151     sim = setup_simulation(v)
152     ds, m = sim.make_mesh(v)
153     y = sim.simulate(m, v)

```

Listing E.1: Python script